The PHANGS-AstroSat Atlas of Nearby Star-forming Galaxies

Hamid Hassani, Erik Rosolowsky, Eric W. Koch, Joseph Postma, Joseph Nofech, Harrisen Corbould, David Thilker, Adam K. Leroy, Eva Schinnerer, Francesco Belfiore, et al.

The Astrophysical Journal Supplement Series, 271:2 (27pp), 2024 March https://doi.org/10.3847/1538-4365/ad152c

The PHANGS-AstroSat Atlas of Nearby Star-forming Galaxies

Hamid Hassani[1], Erik Rosolowsky[1], Eric W. Koch[1,2], Joseph Postma[3], Joseph Nofech[1], Harrisen Corbould[1], David Thilker[4], Adam K. Leroy[5], Eva Schinnerer[6], Francesco Belfiore[7], Frank Bigiel[8], Médéric Boquien[9], Mélanie Chevance[10,34], Daniel A. Dale[11], Oleg V. Egorov[12], Eric Emsellem[13,14], Simon C. O. Glover[15], Kathryn Grasha[16,17,35], Brent Groves[18], Kiana Henny[11], Jaeyeon Kim[19], Ralf S. Klessen[15,20], Kathryn Kreckel[21], J. M. Diederik Kruijssen[22,34], Janice C. Lee[23,24], Laura A. Lopez[25,26], Justus Neumann[27], Hsi-An Pan[28], Karin M. Sandstrom[29], Sumit K. Sarbadhicary[5,26,30], Jiayi Sun[31,32], and Thomas G. Williams[33]

[1] Dept. of Physics, University of Alberta, 4-183 CCIS, Edmonton, Alberta, T6G 2E1, Canada; hhassani@ualberta.ca
[2] Center for Astrophysics | Harvard & Smithsonian, 60 Garden St., Cambridge, MA 02138, USA
[3] Dept. of Physics and Astronomy, University of Calgary, Calgary, AB T2N 1N4, Canada
[4] Center for Astrophysical Sciences, The Johns Hopkins University, Baltimore, MD 21218, USA
[5] Department of Astronomy, The Ohio State University, Columbus, OH 43210, USA
[6] Max Planck Institut für Astronomie, Königstuhl 17, D-69117 Heidelberg, Germany
[7] INAF—Osservatorio Astrofisico di Arcetri, Largo E. Fermi 5, I-50125, Florence, Italy
[8] Argelander-Institut für Astronomie, Universität Bonn, Auf dem Hügel 71, D-53121 Bonn, Germany
[9] Instituto de Alta Investigación, Universidad de Tarapacá, Casilla 7D, Arica, Chile
[10] Zentrum für Astronomie der Universität Heidelberg, Institut für Theoretische Astrophysik, Albert-Ueberle-Str. 2, D-69120 Heidelberg, Germany
[11] Department of Physics & Astronomy, University of Wyoming, Laramie, WY 82071 USA
[12] Astronomisches Rechen-Institut, Zentrum für Astronomie der Universität Heidelberg, Mönchhofstr. 12-14, D-69120 Heidelberg, Germany
[13] European Southern Observatory, Karl-Schwarzschild-Straße 2, D-85748 Garching, Germany
[14] Univ Lyon, Univ Lyon1, ENS de Lyon, CNRS, Centre de Recherche Astrophysique de Lyon UMR5574, F-69230 Saint-Genis-Laval France
[15] Universität Heidelberg, Zentrum für Astronomie, Institut für Theoretische Astrophysik, Albert-Ueberle-Str. 2, D-69120, Heidelberg, Germany
[16] Research School of Astronomy and Astrophysics, Australian National University, Canberra, ACT 2611, Australia
[17] ARC Centre of Excellence for All Sky Astrophysics in 3 Dimensions (ASTRO 3D), Australia
[18] International Centre for Radio Astronomy Research, University of Western Australia, 7 Fairway, Crawley, 6009 WA, Australia
[19] Kavli Institute for Particle Astrophysics & Cosmology (KIPAC), Stanford University, CA 94305, USA
[20] Universität Heidelberg, Interdisziplinäres Zentrum für Wissenschaftliches Rechnen, Im Neuenheimer Feld 205, D-69120 Heidelberg, Germany
[21] Astronomisches Rechen-Institut, Zentrum für Astronomie der Universität Heidelberg, Mönchhofstraße 12-14, D-69120 Heidelberg, Germany
[22] Technical University of Munich, School of Engineering and Design, Department of Aerospace and Geodesy, Chair of Remote Sensing Technology, Arcisstr. 21, D-80333 Munich, Germany
[23] Space Telescope Science Institute, 3700 San Martin Dr., Baltimore, MD 21218, USA
[24] Steward Observatory, University of Arizona, Tucson, AZ 85712, USA
[25] Department of Astronomy, The Ohio State University, 140 W. 18th Ave., Columbus, OH 43210, USA
[26] Center for Cosmology and AstroParticle Physics, The Ohio State University, 191 W. Woodruff Ave., Columbus, OH 43210, USA
[27] Max-Planck-Institut für Astronomie, Königstuhl 17, D-69117 Heidelberg, Germany
[28] Department of Physics, Tamkang University, No. 151, Yingzhuan Rd., Tamsui District, New Taipei City 251301, Taiwan
[29] Department of Astronomy & Astrophysics, University of California, San Diego, 9500 Gilman Dr., La Jolla, CA 92093, USA
[30] Department of Physics, The Ohio State University, Columbus, OH 43210, USA
[31] Department of Physics and Astronomy, McMaster University, 1280 Main St. W., Hamilton, ON L8S 4M1, Canada
[32] Canadian Institute for Theoretical Astrophysics (CITA), University of Toronto, 60 St George St., Toronto, ON M5S 3H8, Canada
[33] Sub-department of Astrophysics, Department of Physics, University of Oxford, Keble Rd., Oxford OX1 3RH, UK
Received 2023 October 13; revised 2023 December 6; accepted 2023 December 7; published 2024 February 12

Abstract

We present the Physics at High Angular resolution in Nearby GalaxieS (PHANGS)-AstroSat atlas, which contains UV imaging of 31 nearby star-forming galaxies captured by the Ultraviolet Imaging Telescope on the AstroSat satellite. The atlas provides a homogeneous data set of far-UV and near-UV maps of galaxies within a distance of 22 Mpc and a median angular resolution of $1\farcs4$ (corresponding to a physical scale between 25 and 160 pc). After subtracting a uniform UV background and accounting for Milky Way extinction, we compare our estimated flux densities to GALEX observations, finding good agreement. We find candidate extended UV disks around the galaxies NGC 6744 and IC 5332. We present the first statistical measurements of the clumping of the UV emission and compare it to the clumping of molecular gas traced with the Atacama Large Millimeter/submillimeter Array (ALMA). We find that bars and spiral arms exhibit the highest degree of clumping, and the molecular gas is even more clumped than the far-UV (FUV) emission in galaxies. We investigate the variation of the ratio of observed FUV to Hα in different galactic environments and kiloparsec-sized apertures. We report that $\sim$65% of the variation of the $\log_{10}$(FUV/Hα) can be described through a combination of dust attenuation with star formation history parameters. The PHANGS-AstroSat atlas enhances the multiwavelength coverage of our sample, offering a

[34] Cosmic Origins Of Life (COOL) Research DAO, https://coolresearch.io/.
[35] ARC DECRA Fellow.

detailed perspective on star formation. When integrated with PHANGS data sets from ALMA, the Very Large Telescope-MUSE, the Hubble Space Telescope, and JWST, it develops our comprehensive understanding of attenuation curves and dust attenuation in star-forming galaxies.

Unified Astronomy Thesaurus concepts: Molecular gas (1073); Interstellar medium (847); Ultraviolet astronomy (1736); Stellar astronomy (1583)

1. Introduction

The high-mass stellar population of a galaxy plays a central role in galactic evolution. High-mass stars, which are short-lived and must have formed recently, change the colors of galaxies and provide the mechanical feedback and radiative feedback that determine the future evolution of the system (Krumholz et al. 2014). Beyond the Local Group, our study of these young, massive stars relies on their photospheric emission, which is directly traced in the near-UV (NUV) and far-UV (FUV) and indirectly observed using recombination line emission in the optical (e.g., Hα) and reprocessing from dust (Kennicutt & Evans 2012).

Studying UV emission from nearby extragalactic targets traces star formation over a longer timescale (100–200 Myr) in comparison to other typical tracers, such as recombination lines (5–20 Myr; Kennicutt & Evans 2012). To understand the UV spectral behavior of young stellar populations located beyond the optical disk, both large field-of-view (FOV) and multiband UV imaging are essential. The latter feature is a key to constraining the attenuation properties, along with the UV color (Decleir et al. 2019). Moreover, because of its sensitivity to small numbers of high-mass stars, UV emission provides a good tracer of star formation beyond optical disks (Thilker et al. 2007) and more generally in galactic environments characterized by low density (Lee et al. 2011), such as dwarf galaxies. Studying short-lived massive stars in the low-density outskirts of galaxies constrains how gas may accrete into galaxies and which mechanism is responsible for the regulation of star formation in these low-column-density environments (Gil de Paz et al. 2007b).

Over the past decades, several telescopes, such as the Galaxy Evolution Explorer (GALEX) and the Neil Gehrels Swift Observatory's Ultraviolet Optical Telescope (UVOT), have mapped UV bands in nearby galaxies (Lee et al. 2011; Rampazzo et al. 2017; Leroy et al. 2019). GALEX provided imaging in the NUV (2500 Å) and FUV (1500 Å), with an FOV of $\sim 1.^{\circ}28$ and an angular resolution of 4″–6″ (Martin et al. 2005). On the other hand, Swift-UVOT has three UV bands with a smaller FOV (17′) and an angular resolution of $\sim 2.''5$ (Roming et al. 2005). Many insights about nearby galaxy populations have been derived from GALEX, combined with multiwaveband results, which have provided a rich understanding of galaxy evolution and the impacts of star formation (e.g., Gil de Paz et al. 2007a; Salim et al. 2007; Leroy et al. 2008; Lee et al. 2009).

The Ultraviolet Imaging Telescope (UVIT) on the AstroSat mission offers an improvement in resolution for imaging energetic UV photons with multiple UV bands. It extends the legacy of GALEX/SWIFT by effectively resolving the structures of star-forming regions, thanks to its $<1.''8$ resolution (Kumar et al. 2012; Singh et al. 2014). UVIT observes in nine bands, covering the range from 1480 to 2790 Å, with a 28′ FOV (Rahna et al. 2017). UVIT data provide a new view of the resolved properties of faint stellar populations beyond the optical disk of galaxies and offer detailed additional information on the UV color and properties of the underlying stellar population.

The UV filter set of the AstroSat UVIT instrument consists of one narrowband filter (N279N), three wideband filters (F148W, F154W, and N242W), and five medium-band filters (F169M, F172M, N219M, N245M, and N263M), where the filter names follow the Hubble Space Telescope (HST) convention that the three digit number represents the central wavelength in nanometers. These filters capture photospheric emission from stellar populations with transmission curves, as shown in Figure 1 (Leahy et al. 2022a, 2022b). The data from AstroSat UVIT can be utilized to discern and model both the age and mass of young stellar populations, ranging from approximately 5–200 Myr and with masses greater than $10^{3-4} M_{\odot}$ (e.g., Ujjwal et al. 2022). Many of these populations are located beyond R_{25}, i.e., the radius at which the surface brightness falls below 25 magnitudes per square arcsecond in the B band.

Sensitive, widefield UV observations are even more powerful when combined with probes of the different phases of the interstellar medium (ISM) and stellar populations. The star formation process, as traced by the NUV and FUV, offers valuable insight when aligned with other tracers of star formation phases. CO observations, which trace molecular gas, identify dust-shrouded star-forming regions, areas where UV photons can quickly destroy clumps. Observations of ionized gas, captured through hydrogen recombination lines, showcase the re-emission stemming from the extreme UV (EUV) of the highest-mass stars.

Integrating the UV observations from nearby galaxies with a spatial resolution below 200 pc can enhance the comprehensive understanding advanced by projects like the Physics at High Angular resolution in Nearby GalaxieS (PHANGS) collaboration. The PHANGS-Atacama Large Millimeter/submillimeter Array (ALMA) survey (Leroy et al. 2021) yielded $\sim 1''$ resolution observations of CO(2−1) emission from molecular clouds in 90 nearby galaxies. Similarly, PHANGS-MUSE used Very Large Telescope (VLT)/MUSE observations to map out optical emission lines from 19 of the 90 ALMA targets, also at $\lesssim 1''$ resolution. PHANGS-AstroSat provides an essential complement to the UV imaging obtained by the PHANGS-HST survey (Lee et al. 2022), which only probes to $\sim$2500 Å, but achieves an angular resolution of $0.''08$ over the smaller FOVs of the WFC3 camera. In this work, we compare the new UV data to these other tracers of the star formation process to understand how galaxies evolve at these arcsecond scales.

One of the main drivers of galaxy evolution is the relationship between gas and star formation, called the Kennicutt–Schmidt (KS) relation (Kennicutt 1998), which presents a tight correlation between the surface densities of gas and star formation on large scales (>1 kpc) in galaxies. However, several studies indicate that this relation operates on kiloparsec scales and it may break down at smaller scales (e.g., Bigiel et al. 2008; Kruijssen et al. 2019). While these results typically rely on recombination line tracers of star formation,

Table 1
PHANGS-AstroSat Galaxies

Galaxy	Observation ID	PI[a]	Observation Date	Filter(s)
IC 5332	A07_027T02_9000003258	rosolowsky	2019 Oct 26	F148W
	A07_027T02_9000003640	rosolowsky	2020 May 4	F148W
NGC 0253	G0685_010T01_9000001672	jmurthy	2017 Nov 8	F169M, N245M
	G0685_031T01_9000001702	askpati	2017 Nov 19	F169M, N219M, N263M
NGC 0300	G05_235T01_9000000590	hutchingsj	2016 Aug 11	F148W, F154W, F169M, F172M, N219M, N245M, N263M
NGC 0628	A04_209T01_9000002378	carobert	2018 Sep 20	F154W, F172M
	G06_151T01_9000000836	askpati	2016 Nov 29	F148W, F154W, F169M, F172M, N242W, N219M, N245M, N263M, N279N
NGC 1097	A10_021T01_9000004044	rosolowsky	2020 Dec 2	F148W
NGC 1300	A07_027T05_9000003506	rosolowsky	2020 Feb 16	F148W
NGC 1317	A04_164T01_9000001770	nilkanth	2017 Dec 14	F148W, F154W, F169M, F172M, N219M
NGC 1365	A02_006T01_9000000776	gulabd	2016 Nov 8	F169M, N279N
	A02_006T01_9000000802	gulabd	2016 Nov 17	F148W, F169M, N279N
	A02_006T01_9000000934	gulabd	2016 Dec 28	F169M, N279N
	G07_057T02_9000001504	stalin	2017 Aug 31	F148W, F172M, N219M, N263M
NGC 1385	A07_027T06_9000003508	rosolowsky	2020 Feb 16	F148W
NGC 1433	G07_066T01_9000001510	swarna	2017 Sep 1	F154W, F169M, N219M, N245M, N263M, N279N
NGC 1512	G06_135T01_9000000908	swarna	2016 Dec 21	F154W, N245M, N263M
	G07_068T01_9000001502	kanak	2017 Aug 30	F154W, N242W
NGC 1546	A07_010T11_9000003240	rrampazzo	2019 Oct 17	F148W
NGC 1566	G06_087T01_9000000926	stalin	2016 Dec 26	F148W, F172M, N219M, N263M
	T02_085T01_9000002296	gulabd	2018 Aug 11	F154W
	T03_020T01_9000002444	gulabd	2018 Oct 22	F154W
NGC 2090	A05_155T02_9000003200	mousumi	2019 Sep 24	F148W
NGC 2835	T03_032T01_9000002564	rosolowsky	2018 Dec 14	F148W
NGC 2903	G08_031T03_9000001972	askpati	2018 Mar 12	F148W, F169M, N219M, N263M
NGC 3351	T03_034T01_9000002500	rosolowsky	2018 Nov 10	F148W
NGC 3621	G08_083T03_9000002022	stalin	2018 Apr 7	F148W, F172M
NGC 3627	T03_033T01_9000002568	rosolowsky	2018 Dec 15	F148W
NGC 4254	A08_003T04_9000003634	hutchingsj	2020 May 2	F148W
NGC 4298	A10_021T04_9000004116	rosolowsky	2021 Jan 17	F148W
NGC 4321	A08_003T05_9000003426	hutchingsj	2020 Jan 11	F154W
NGC 4476	G06_051T01_9000000972	pcote_nrc	2017 Jan 22	F154W, N242W
NGC 4535	A10_021T06_9000004338	rosolowsky	2021 Apr 27	F148W
NGC 4571	G06_016T01_9000001052	kanak	2017 Feb 25	F154W, N263M
NGC 4579	A08_003T09_9000003644	hutchingsj	2020 May 5	F154W
NGC 4654	A07_027T12_9000003664	rosolowsky	2020 May 13	F148W
	A08_003T08_9000003638	hutchingsj	2020 May 3	F154W
NGC 5128	G08_023T01_9000001978	sreekumar	2018 Mar 15	F148W, N219M, N245M, N279N
NGC 6744	A05_022T09_9000003058	rosolowsky	2019 Jul 24	F148W
	A10_021T10_9000004210	rosolowsky	2021 Feb 26	F148W
NGC 7496	A07_027T16_9000003222	rosolowsky	2019 Oct 5	F148W
	A07_027T16_9000003642	rosolowsky	2020 May 5	F148W
	A07_027T16_9000003666	rosolowsky	2020 May 14	F148W
NGC 7793	G06_024T01_9000000780	annapurni	2016 Nov 10	F148W, N242W

Note.
[a] The PIs listed here are directly read from the AstroSat Archive Search system. The "Filter(s)" column shows all available filters as presented on AstroSat Archive Search; we do not necessarily utilize calibrated data for every single listed filter for each galaxy.

AstroSat imaging can play a key role in estimating the link between star formation and the amount of molecular gas over longer timescales. UV observation can make progress even in the outskirts of galaxies, where the fraction of molecular relative to neutral gas is low. However, we should note that simulations such as those by Khoperskov & Vasiliev (2017) have shown that the relation between UV-based star formation rates (SFRs) and the total amount of gas at 50 pc resolution is unclear, and observations suggest that the KS relation prescription cannot be extrapolated to the low-density environments of outer galaxy disks (Dessauges-Zavadsky et al. 2014). These findings underscore the need for high-resolution investigations of UV-based star formation processes beyond the optical disks of galaxies.

The relationship between UV and Hα luminosities provides valuable information on dust content, the age of stellar populations, and the metallicity of galaxies. Previous studies (e.g., Lee et al. 2009, 2011) have attempted to uncover the details of the UV–Hα relation, with a focus on understanding recipes for the integrated SFR in galaxies. However, the dependence of this relation on the actual amount of molecular gas and dust reddening remains unclear. Furthermore, there is a lack of detailed information on how the ratio changes across different environments within galaxies, such as bars, centers,

Table 2
PHANGS-AstroSat Exposures

Galaxy	F148W (ks)	F154W (ks)	F172M (ks)	F169M (ks)	N242W (ks)	N245M (ks)	N263M (ks)	N219M (ks)	N279N (ks)
IC 5332	2.28[a]	...	...	...	...	...	...	...	...
NGC 0253	...	...	...	12.29	...	12.40	3.02	4.57	...
NGC 0300	12.84	1.65	0.95	6.92	...	2.74	2.52	0.32	...
NGC 0628	1.82	4.88	19.12	2.42	0.43	1.32	2.08	1.36	4.65
NGC 1097	1.75[a]	...	...	...	...	...	...	...	...
NGC 1300	3.44[a]	...	...	...	...	...	...	...	...
NGC 1317	0.83	1.01	0.87	1.41	...	...	...	4.32	...
NGC 1365	2.10	...	6.59	46.03	...	...	2.07	6.53	47.39
NGC 1385	1.79[a]	...	...	...	...	...	...	...	...
NGC 1433	...	3.14	...	3.17	...	1.67	0.91	3.20	1.25
NGC 1512	...	5.80	...	...	3.70	1.02	1.20	...	...
NGC 1546	6.65	...	...	...	...	...	...	...	...
NGC 1566	2.94	3.38	1.34	...	...	...	2.96	1.37	...
NGC 2090	6.43	...	...	...	...	...	...	...	...
NGC 2835	3.41[a]	...	...	...	...	...	...	...	...
NGC 2903	3.50	...	...	4.32	...	...	3.35	4.61	...
NGC 3351	2.64[a]	...	...	...	...	...	...	...	...
NGC 3621	2.10	...	6.37	...	...	...	...	...	...
NGC 3627	3.17[a]	...	...	...	...	...	...	...	...
NGC 4254	...	7.60	...	...	...	...	...	...	...
NGC 4298	2.92[a]	...	...	...	...	...	...	...	...
NGC 4321	...	7.63	...	...	...	...	...	...	...
NGC 4476	...	35.88	...	...	35.21	...	...	...	...
NGC 4535	1.21[a]	...	...	...	...	...	...	...	...
NGC 4571	...	9.58	...	...	...	...	9.65	...	...
NGC 4579	...	7.59	...	...	...	...	...	...	...
NGC 4654	3.52[a]	...	...	...	...	...	...	...	...
NGC 5128	23.31	...	...	...	...	4.75	...	10.53	8.00
NGC 6744	3.45[a]	...	...	...	...	...	...	...	...
NGC 7496	6.16[a]	...	...	...	...	...	...	...	...
NGC 7793	7.53	...	...	...	8.10	...	...	...	...

Note.
[a] Observed as a part of the PHANGS-AstroSat request.

and spiral arms at small scales. The ionized gas traced by Hα and observed through MUSE/VLT observations with the PHANGS-MUSE survey offers a new perspective on recent star formation up to 10 million yr ago as well as dust reddening (Emsellem et al. 2022). When combined with the new UVIT observations, we will be able to directly relate the changing UV to Hα to the local environment in these galaxies.

In this paper, we present a homogeneous data set of UV images of 31 nearby galaxies observed by AstroSat in the wavelength range of 1480–2790 Å. Our main focus is to reduce and assess the quality of the data set and compare it with previous low-resolution observations. Additionally, we study the variation of the UV and molecular gas clumpiness in different morphological regions of galaxies. By comparing the FUV to the Hα flux in different galaxies, we aim to provide predictive models for the ratio in different environments. This work is expected to contribute to the interpretation of different tracers of star formation at high resolution ($<$200 pc) and provide a quantitative framework for the relation between UV and Hα luminosity.

In Section 2.1, we present our sample selection strategies and then the observations. We focus on the reduction and quality assessment of our data in Section 3. Then, we present two extended UV (XUV) disk candidates in Section 4 and provide details about the clumping of UV and CO emission at high resolution ($\lesssim$1.5″) in Section 5. Finally, we compare the luminosity of FUV to Hα emission to show how these two star formation tracers vary in different morphological parts of galaxies and how their ratio depends on dust attenuation, star

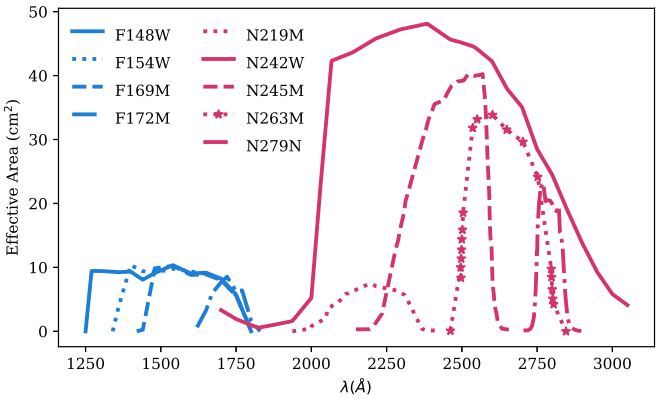

Figure 1. Filters used in the AstroSat UVIT observations, corrected for in-orbit calibrations. The blue lines show the effective area of the FUV bands, whereas the pink lines are the NUV bands.

formation history parameters, and the equivalent width (EW) of the Hα emission (Section 6).

2. Data

2.1. Sample Selection

To maximize the opportunity for multiwavelength science, we selected galaxies that have been observed as part of the PHANGS survey for observation using AstroSat. The primary PHANGS sample consists of 90 nearby galaxies observed with ALMA (Leroy et al. 2021) in molecular line emission. These targets are selected to be nearby ($D < 22$ Mpc), so a high-efficiency observation with ALMA yields high-quality maps of the molecular ISM with $\sim 1''$ resolution. The proximity of the targets means that the $1''$ resolution translates into small physical scales, providing a robust census of star-forming galaxies at ~ 100 pc linear resolution, which matches the typical scale heights of galaxies (Sun et al. 2020) and the size of giant molecular clouds (Rosolowsky et al. 2021). The PHANGS targets are relatively massive ($10^{9.75} < M_\star/M_\odot < 10^{11.0}$) and mostly lie on the star-forming main sequence, with $\mathrm{SFR}/M_\star > 10^{-11}\,\mathrm{yr}^{-1}$. The sample was selected with a constraint to avoid highly inclined systems, ensuring that $i < 75°$. Table 3 presents the 31 galaxies in the PHANGS-AstroSat sample and their properties, adopted from Leroy et al. (2021).

2.2. Observations

The AstroSat satellite mission provides observations from four instruments: the Large Area X-ray Proportional Counter, the Cadmium Zinc Telluride Imager, the Soft X-ray Telescope, and UVIT (Kumar et al. 2012), which is the primary instrument used in this study. The main goal of UVIT is imaging in the FUV (1300−1800 Å) and NUV (2000−3000 Å), with an FOV of $\sim 28'$. We observed 11 of the 31 selected galaxies under programs T03-032, T03-033, A05-022, A07-027, A08-003, and A10-021. The PHANGS-AstroSat observations adopted a uniform strategy for the primary sample, requesting 3.6 ks of time on each target in the F148W filter. However, instrumental fluctuations and orbital accessibility limited the actual time acquired to 1–3 ks. We supplement these observations with additional archival data for 20 PHANGS targets, identified from the AstroSat Archive.[36] As the supplementary data come from various observing programs, they use different observational strategies and exposures. Archival observations feature a variety of adopted filters and exposure times, some of which may be longer than those proposed for our observations. For instance, NGC 4476 has an exposure time that is 10 times longer than most of the sample. During UVIT observations, AstroSat consistently records data from other instruments within its focal plane. While we do not present these data in this work, they are accessible directly from the archive.

The combination of archival and dedicated observations leads to heterogeneous data across the 31 galaxies. Table 1 summarizes the available AstroSat observations in this atlas, including the observation IDs, dates of observations, and the observed filter set, as illustrated in Figure 1. This table includes allocated projects led by our team, as well as data sets retrieved from the archive. Table 2 summarizes the exposure times for the different galaxies across the different filter sets. We describe the data processing for UVIT in Section 3.

[36] https://astrobrowse.issdc.gov.in/astro_archive/archive/Home.jsp

2.3. Ancillary Data

Besides the AstroSat FUV and NUV observations, we also use several data sets from the literature and from the PHANGS-ALMA and PHANGS-MUSE surveys, which we summarize below.

2.3.1. PHANGS-ALMA

We used CO(2−1) emission-line maps from the PHANGS-ALMA project (Leroy et al. 2021). The emission lines were observed at the rest frequency of $\nu = 230.538$ GHz (Band 6), where the combination of receiver sensitivity and atmospheric transparency makes ALMA most efficient for $1''$ scale mapping of molecular gas. The ALMA data set provides a unique, $\sim 1''$ (100 pc at 20 Mpc) view of nearby main-sequence galaxies at giant molecular cloud scale. The median of the 1σ noise in the cube of all targets is estimated to be 6.2 mJy beam^{-1} at native resolution (corresponding to a brightness temperature of ~ 0.17 K). The velocity resolution of 2.5 km s^{-1} is chosen to improve the signal-to-noise ratio (S/N) and quality of the deconvolution process. These observations were conducted using a bandwidth of 937.5 MHz with a channel width of $\Delta\nu = 244$ kHz. In contrast to UV observations from AstroSat, ALMA maps only cover the IR-bright portion of the inner disk ($R_{\mathrm{gal}} = 5$–6 kpc) of our targets. Final data products are released using two different masks, both indicating the likely location of real CO emission inside each cube. In this study, we used a high-completeness "broad" mask, which is better for the detection of diffuse emission from the galaxy. The broad mask is built by convolving the cube into several lower-resolution cubes and then creating a mask. Along with the zero-moment maps that we used in this study, the uncertainty maps are also provided, based on a three-dimensional noise model (Leroy et al. 2021, their Section 7.2).

2.3.2. PHANGS-MUSE

We also utilized products from PHANGS-MUSE (program IDs: 1100.B-0651/PI: E. Schinnerer; 095.C-0473/PI: G. Blanc; and 094.C-0623/PI: K. Kreckel). This sample encompasses 19 nearby star-forming spiral galaxies, as described by Emsellem et al. (2022). Of these, 15 targets are also included in the PHANGS-AstroSat observations. The entire program took a total telescope time of ~ 172 hr and each target has been observed with 3 to 15 pointings to cover the disk of the galaxy. Observations were conducted using the MUSE widefield mode (FOV = $1'$), using the nominal (nonextended) wavelength from 4800 to 9300 Å. The spectral resolution varies with wavelength, but is typically around 2.75 Å (full width at half maximum or FWHM). The median point-spread function (PSF) of the sample has a $0\farcs69$ FWHM at 6483.5 Å. We use the emission-line maps from Emsellem et al. (2022), which are created through the MUSE Data Analysis Pipeline that fits each emission line along with the properties of the underlying stellar continuum. In this work, we use the Hα and Hβ emission lines, as well as an estimate of the light-weighted stellar population ages determined from fits to the stellar spectra (Emsellem et al. 2022).

2.3.3. Literature Data Sets

Finally, we use the IR and UV maps of our targets provided by Leroy et al. (2019), who supply an atlas of WISE (3.4 to 22 μm) and GALEX UV maps of ∼15,000 nearby galaxies ($D \leqslant 50$ Mpc). These GALEX maps are background-subtracted for UV background emission and corrected for foreground Galactic extinction. In our quality assessment analysis, we employ GALEX maps that are convolved to an angular resolution of 7.″5, in accordance with the Leroy et al. (2019) data set.

3. AstroSat Data Processing

The Level 1 data products were generated using v2.1 and v2.2 of the AstroSat pipeline from Ravishankar et al. (2021), depending on the data set, and the Level 2 data were processed with the CCDLAB software package (Postma & Leahy 2017). The pipeline accounts for various instrumental effects, such as spacecraft drifts, jitter, and thermal effects. A bright white dwarf (HZ4) was adopted as a photometric calibration source. A detailed set of criteria for selecting this source is discussed by Tandon et al. (2017). The intensity of an image is converted from the observed counts per second (CPS) to the flux density per 0.″42 size pixel (F_λ) using the updated in-orbit calibrations, following

$$F_\lambda(\mathrm{erg\ s^{-1}\ cm^{-2}\ \AA^{-1}}) = \mathrm{CPS} \times \mathrm{UC}, \quad (1)$$

where UC is the unit conversion factor derived from the zero-point magnitude in the AB system as (Tandon et al. 2020, their Table 3):

$$\mathrm{UC} = 10^{-0.4\frac{(\mathrm{ZP}+2.407)}{\lambda^2_{\mathrm{mean}}}}. \quad (2)$$

The λ_{mean} corresponds to the mean wavelengths of the UVIT filters in angstroms. The uncertainties in F_λ for different filters are due to the Poisson noise of the photon-counter detector as well as to uncertainties in the UC factors (Subramaniam et al. 2016). In this study, we only propagate the uncertainty in CPS, as the UC errors are taken to be small. These uncertainties yield 5% uncertainty in the flux density for each filter (Singh et al. 2021). We align each image along the cardinal directions by reprojecting with the REPROJECT Python package.[37] Because the PSF is minimally sampled, we found that the adaptive resampling method was sufficient to maintain flux conservation in the reprojected image. Other interpolation and flux conserving methods produced a Moiré artifact pattern in the reprojected image, which was also noted by Clark et al. (2018), where they increased the pixel size in the reprojected image to avoid this artifact. Using the adaptive resampling method in REPROJECT, we can maintain the same pixel scales as the original images. The final images have a pixel size of 0.″42. As an example, we show a large panel of the NGC 1566 FUV (F148W) map, with environmental masks adopted from Querejeta et al. (2021) in different colors and 1 kpc size hexagonal apertures, in Figure 2. We show the rest of the PHANGS-AstroSat targets at the FUV band in Figures 3 and 4, with contours from CO(2−1) molecular gas. In this study, we refer to FUV data specifically as data from the F148W band, which is the most available filter. Whenever the F148W-band data are not available, we use other bands. Most galaxies have observations in the F148W filter, except NGC 1433, NGC 1512, NGC 4321, NGC 4571, NGC 4476, NGC 4579, and NGC 4254, which are in the F154W filter. In the case of NGC 0253, the only FUV band available is F169M.

[37] https://reproject.readthedocs.io/en/stable/

3.1. Background Subtraction

FUV imaging shows a near constant flux of emission from "blank" sky, which we refer to as the *background*, even though much of this emission may be from Galactic and solar system sources (Kulkarni 2022). Taking advantage of the large FOV of the AstroSat observations, we have a radial profile of each object that extends beyond ∼30 kpc galactocentric distance for most of the targets. We estimate the background by assuming the galaxy emission profile is an exponential disk (e.g., Regan et al. 2001) and include a constant background term:

$$S_\lambda = S_0\, e^{(-R_{\mathrm{gal}}/\gamma)} + B_\lambda, \quad (3)$$

where S_λ is the emission at different bands, S_0 is the surface brightness at galactocentric radius $R_{\mathrm{gal}} = 0$, γ is the scale length, and B_λ is the background value. We estimate the background emission (B_λ) for all UV bands of AstroSat. The calibrated units of the FUV and NUV maps are in $\mathrm{erg\ s^{-1}\ cm^{-2}\ \AA^{-1}\ pix^{-1}}$, but we present maps scaled to units of $\mathrm{MJy\ sr^{-1}}$ to facilitate comparison to multiwavelength data. For comparison with the UV emission, we apply the same exponential model to the CO emission, fixing $B = 0$, where we use the CO "broad mask" integrated intensity maps from Leroy et al. (2021). This fit to the molecular line emission derives its scale length to compare it with the FUV scale length. We return to the comparison of the FUV CO scale lengths in more detail in Section 4, but here the primary use is to set the background level for the UV emission.

To minimize the impact of the FUV bright central bump commonly found in galaxies, we exclude the bar region from the radial profile by using a radius of $1.3 \times R_{\mathrm{Bar}}$, where R_{Bar} is adopted from Herrera-Endoqui et al. (2015; see also Querejeta et al. 2021). For NGC 4535 and NGC 6744, we adopt bar sizes of 5.1 and 4 kpc, respectively. We determine the radial profiles by averaging the flux in annuli with widths of 500 pc from the center of the galaxy up to a maximum galactocentric distance of <50 kpc. This maximum distance is chosen through visual inspection of different galaxies to exclude any bright nearby sources. Figure 5 presents the radial profiles of the AstroSat observations in the FUV band for IC 5332 and NGC 1566. The remaining radial profiles are presented in the Appendix. In the case of NGC 0253, we use the only available filter in the FUV band: F169M.

For most of our targets, AstroSat's large (28′) FOV includes enough sky area at larger galactocentric distances that our simple exponential model (Equation (3)) is sufficient for determining the background level of images robustly. However, some targets have relatively smaller amounts of empty emission-free sky, due to the small coverage of observations or several bright sources in the FOV. In these cases, regression over the exponential model fails for a few targets. For example, NGC 0300 is sufficiently nearby that we only have a radial profile out to a small galactocentric distance of $R_{\mathrm{gal}} < 12$ kpc. Furthermore, the exponential model is not appropriate for the

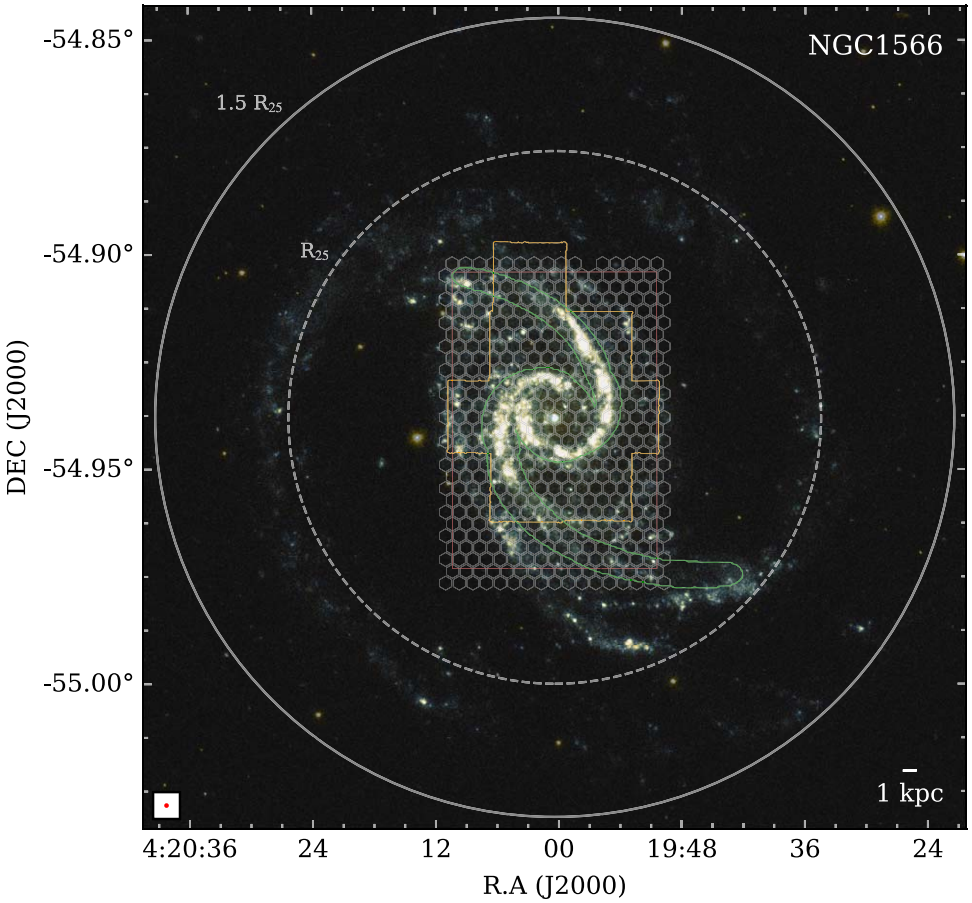

Figure 2. AstroSat UVIT F148W (FUV; blue) and N263M (NUV; yellow) maps of NGC 1566 using an asinh brightness scale. The dynamical range of the N263M image is the same as for the F148W map, but normalized to the F148W/N263M central wavelength ratio for consistent cross-filter comparison. We show circles with radii of R_{25} (dashed line) and 1.5 R_{25} (solid line). The classification of the spiral arms environment (green) is shown on the map. We show the PSF FWHM in the bottom left corner of the map as a red dot and a physical scale of 1 kpc in the bottom right corner. In addition, we plot the 1 kpc size hexagonal apertures that we use to measure several quantities in Sections 5 and 6. We overlay the MUSE/VLT and ALMA footprints in the orange and red colors, respectively.

highly inclined NGC 0253, where we see many bright gas clumps at $R_{\rm gal} < 10$ kpc. In the cases of NGC 3621 and NGC 5128, we decided not to use the regression to determine the background level, due to a number of nearby bright sources. Finally, in the interacting system of NGC 1512-1510, a simple exponential model could not describe the complicated radial profile of this merging system, hence the background value could not be estimated robustly from radial profiles.

In these cases, we instead used a "mean-level" estimate of the backgrounds. The background value for each of these targets is estimated by taking the mean value of an annulus around each object. The annulus radius is provided by visual inspection, ensuring the exclusion of nearby sources, mostly $R > 3\,R_{25}$. However, these annuli values might still suffer from bright stars or reaching the edge of the FOV. We reject bright sources using Chauvenet's criterion in the annulus data distribution (i.e., iteratively rejecting data $>3\sigma$, where σ is the standard deviation, and then recalculating σ). The standard deviation is inserted into the Chauvenet criterion using the median absolute deviation (MAD) as an estimator. The MAD standard deviation is provided by the `astropy.stats` module.[38] Although the MAD standard deviation is robust to outliers, it could be zero or much smaller than the normal standard deviation, due to the faint nature of the background emission. In that case, we use ordinary standard deviation to avoid the failure of the Chauvenet criterion. After rejecting data using this criterion, we estimate the background as the mean in the annulus. Regarding the discussion of the new XUV disk galaxy NGC 6744, which has spiral arms extending beyond 2 R_{25} (as detailed in Section 4), we have decided to avoid using the radial profile or "mean-level" background. The radial profile of this galaxy is not exponential and the estimation of the background is not reliable, due to the presence of numerous bright stellar clusters and H II regions. Therefore, we have carefully chosen a few 1.′5 apertures that are free from bright sources and estimated the mean emission from those locations. The estimated background is 20% and 34% higher than "mean level" and radial profile, respectively.

Table 4 lists the foreground extinction, background values, and scale lengths of our sample for both the FUV band and CO emission.

3.2. Foreground Extinction

As Milky Way foreground dust extinguishes the UV emission of each target, we first corrected both the AstroSat FUV and NUV fluxes for foreground extinction, following the Leroy et al. (2019) procedure. A uniform foreground dust distribution is expected, due to the small angular size of each target. The ratios of total to selective extinction $R_{\rm FUV}$ and $R_{\rm NUV}$

[38] https://docs.astropy.org/en/stable/stats/index.html

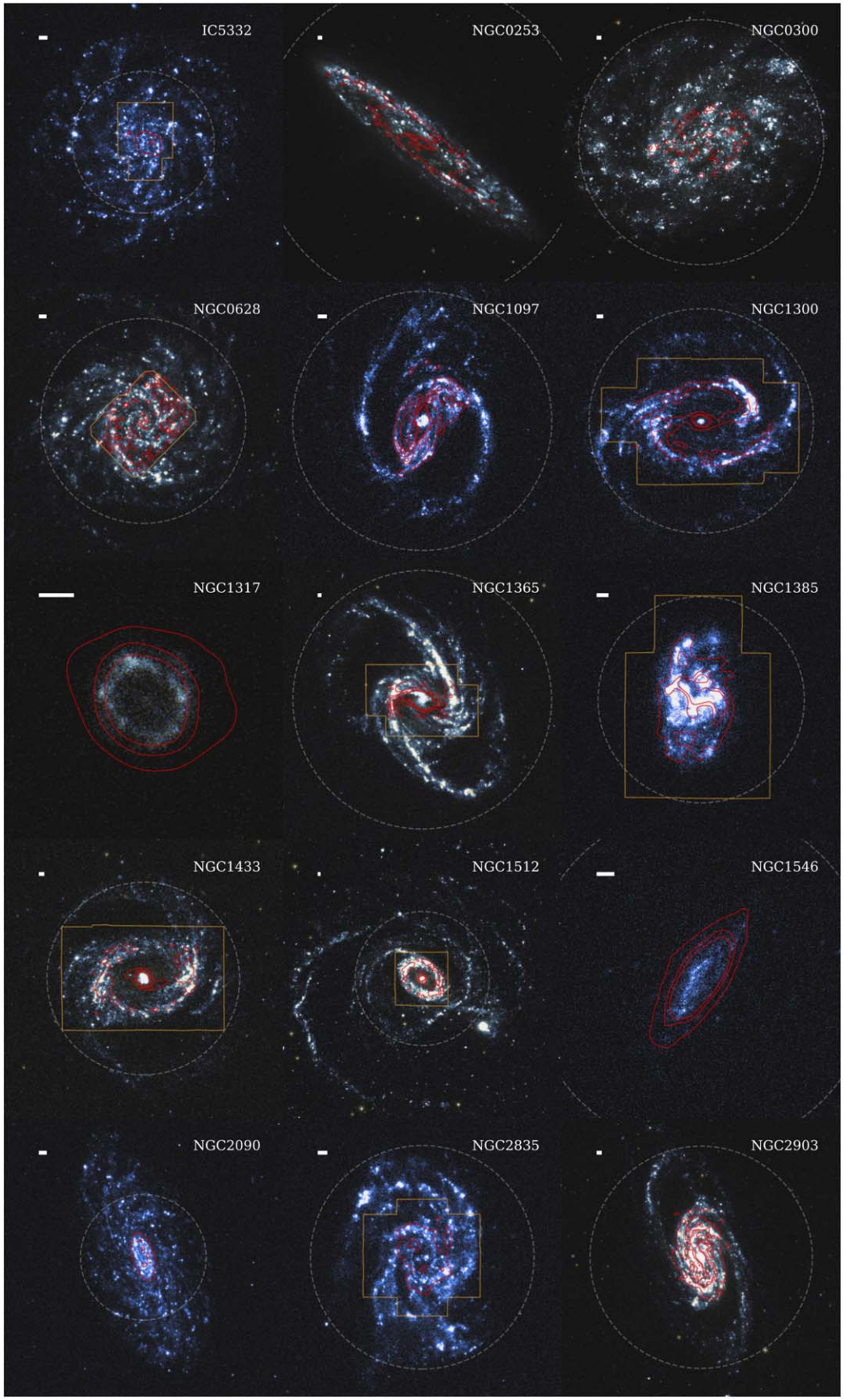

Figure 3. Maps of PHANGS-AstroSat galaxies in the FUV band (blue) and any available NUV band (yellow) on an asinh brightness scale. The dynamical range of the NUV is the same as the FUV map, but normalized to an FUV/NUV central wavelength ratio for consistent cross-filter comparison. The red contours are from ALMA CO(2−1) data from 1 to 10 K km s^{-1}. Both the FUV and CO data are at a common 1.″8 resolution. Galaxies vary in angular and physical size. A radius of R_{25} is shown as a circle with a dashed line. The white lines to the top left of the maps have a length of 1 kpc. We overlay the MUSE/VLT footprints with the orange color.

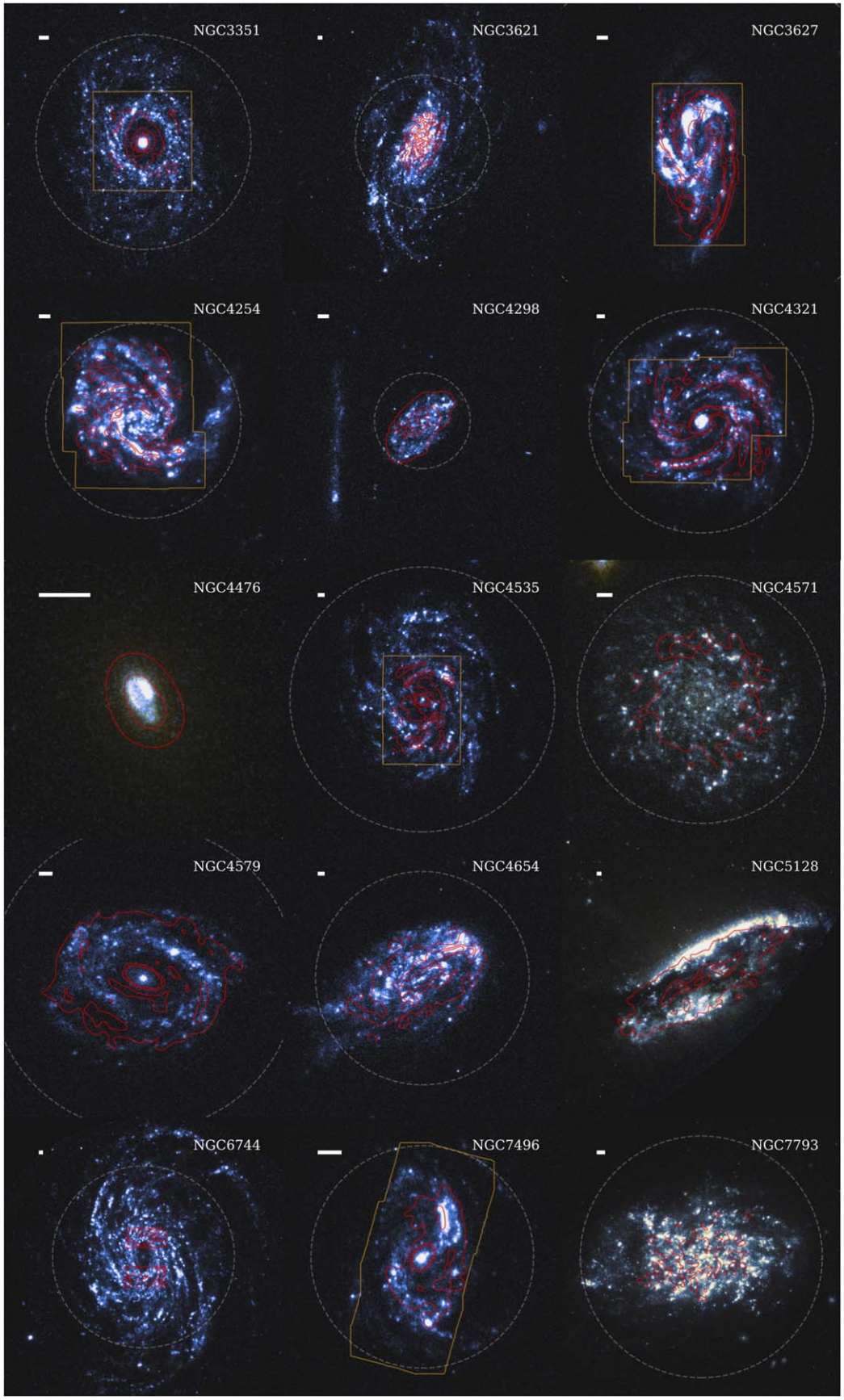

Figure 4. The same as Figure 3, but for NGC 0300, NGC 5128, NGC 0253, and NGC 7793 we use lower-resolution ALMA CO data (Total Power and 7 m; $\sim 8''$), with contours between 0.75–10, 5–100, 5–100, and 1–10 K km s^{-1}, respectively.

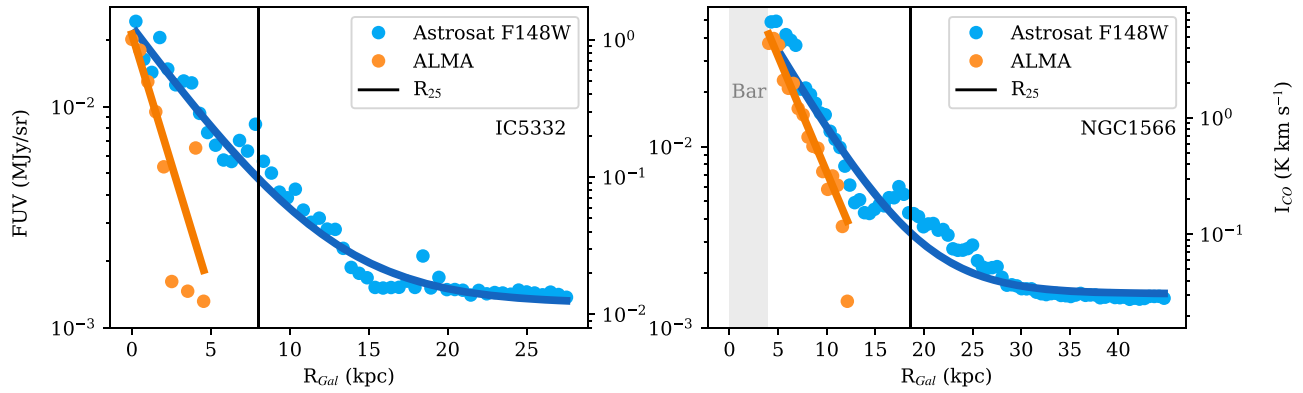

Figure 5. Radial profiles of FUV (blue) and CO (orange) emissions for IC 5332 (left) and NGC 1566 (right). The FUV radial profiles are presented before background subtraction and correction for Milky Way extinction. The black vertical line indicates the position of R_{25} in kiloparsecs, while the gray line represents the maximum length of the bar, as reported by Herrera-Endoqui et al. (2015), which we have excluded from the radial profiles. The solid lines show the exponential fits to the radial profiles as described in the text.

are given by Peek & Schiminovich (2013) as a function of color excess $E(B-V)$. The extinction is estimated using $A_\lambda = R_\lambda E(B-V)$ at the FUV and NUV wavelengths. Based on the Schlegel et al. (1998) dust maps and the $E(B-V)$ value for each galaxy, $A_{\rm FUV}$ and $A_{\rm NUV}$ are estimated for each target in the sample, resulting in a median foreground of $A_{\rm FUV} = 0.21$ mag, but the correction shows $A_{\rm FUV} > 1$ mag for NGC 5128 and NGC 2835.

3.3. Quality Assurance

We characterize the quality of the AstroSat imaging through three separate checks: we assess the resolution by fitting point sources in the data, we validate the alignment against higher-resolution HST data, and we compare the flux scales to archival GALEX maps from Leroy et al. (2019). In all cases, the AstroSat data meet acceptable quality standards.

3.3.1. Resolution and Alignment

We characterize the PSF of the data reduction empirically using point sources in the final reduced products. The PSF of the final data is primarily set by the quality of the tracking solution and alignment of subimages, which can vary based on the brightness of the sources in the field and the number of contributing observations to a final image.

To measure the PSF, we identify the point sources in the image, stack the images, and fit a Moffat PSF model (Moffat 1969) to the resulting image stack. We adopt the Moffat PSF model since it appears to characterize the PSF of bright sources well, including a compact core with extended wings that result from deviations in star tracking. We develop a customized solution to PSF characterization because of the relatively low number of photon counts in an individual source and the relatively small number of stars that are bright in the UV. First, we smooth the image with a Gaussian kernel with a standard deviation of 2 pixels. We then identify point sources using the DAO Star Finder algorithm (Stetson 1987), as implemented in the PHOTUTILS package (Bradley et al. 2020) in PYTHON. Of these candidate sources, we crossmatch to objects identified in Gaia Data Release 3 (DR3; Gaia Collaboration et al. 2023), retaining only those sources within 2″ of a Gaia DR3 source with a parallax/error value of 10 or more. Such sources are likely to be stars in our own Galaxy. These selections yield typically 20–40 sources per field. We stack the extracted sources on the maximum brightness pixel to form a single representative star image and fit a two-dimensional Moffat profile to the resulting stack. The median resolution of the FUV bands is 1.″4 and the median resolution of the NUV bands is 1.″2. The better resolution for the NUV bands comes from the improved tracking of the higher S/N values in the NUV images (Tandon et al. 2017). The derived PSF parameters are recorded in the header of each image in the data release.

We use the astrometric solution implemented in CCDLAB, following the approach outlined in Postma & Leahy (2020). This method identifies UV-bright Gaia sources in the field and fits an astrometric solution. We evaluate the quality of the solution by comparing NUV data (where available) to the F275W filter from the HST imaging (Lee et al. 2022) through cross-correlation. In all cases, we find better than 0.4″ accuracy in the astrometric alignment.

3.3.2. Comparison with GALEX

To validate our reduction, we performed a comparison with GALEX observations. Only a portion of the AstroSat data is comparable with GALEX bands: notably, F148W and F154W in AstroSat can be compared to the GALEX FUV band, and N219M and N242W in AstroSat can be compared to the NUV band. Even these comparisons should be made with caution, due to differences between the widths of filters and their central wavelengths.

The units of the AstroSat maps are converted to MJy sr^{-1} and then we convolve the AstroSat images to a common resolution of 7.″5 and reproject the AstroSat images to match the GALEX observations from Leroy et al. (2019). Pixel values below 5σ rms are masked using the ASTROPY.STATS.SIGMA-CLIPPED-STATS module on GALEX maps. Figures 6 and 7 show the pixel value distributions of the AstroSat-to-GALEX ratio maps, indicating the 25th and 75th percentiles of distribution as the top and bottom of the boxes, as well as the median value (center line). The lines extending from the box indicate the minimum and maximum of the distribution. Using the SKLEARN.LINEAR_MODEL module[39] ordinary least squares regression, we also fit a line to the average of every 30 pixel values, using $Y(\text{Astrosat}) = \beta X(\text{GALEX}) + C$ over data in linear space to obtain a slope to characterize the linear

[39] https://scikit-learn.org/stable/modules/generated/sklearn.linear_model.LinearRegression.html

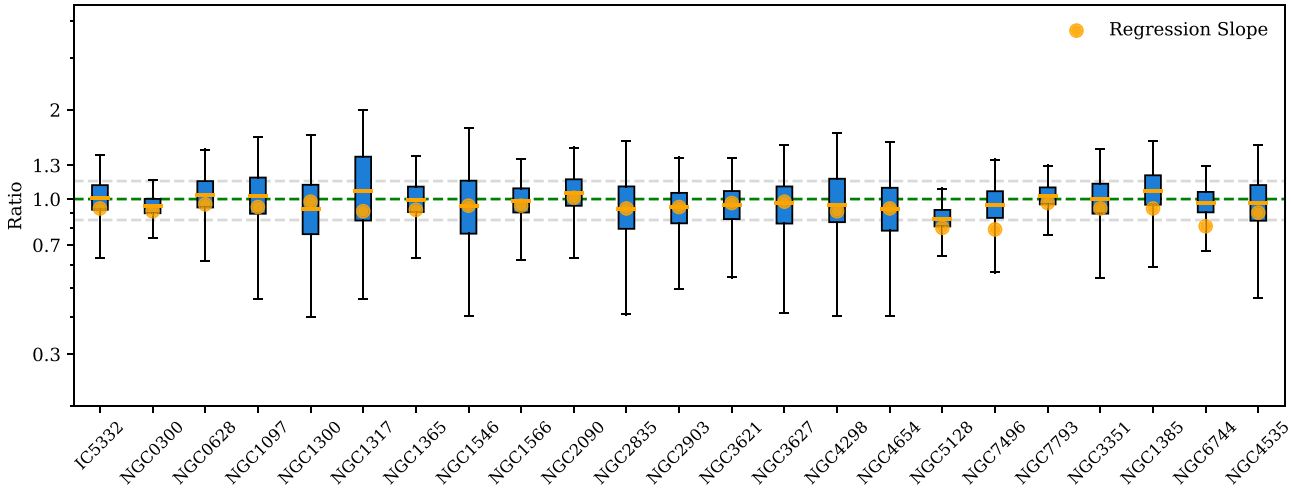

Figure 6. Pixel value distribution of the AstroSat F148W to GALEX FUV maps at a common beam of 7.″5 for different galaxies. The *y*-axis is plotted in a log scale. Both maps are background-subtracted and corrected for Milky Way foreground extinction using the same approach. The green dashed line is the ratio of unity and the gray horizontal lines show confidence bands of 15%. The slopes of regression between pixel values of the GALEX and AstroSat maps (described in Section 3.3.2) are shown as the orange points on the box plots.

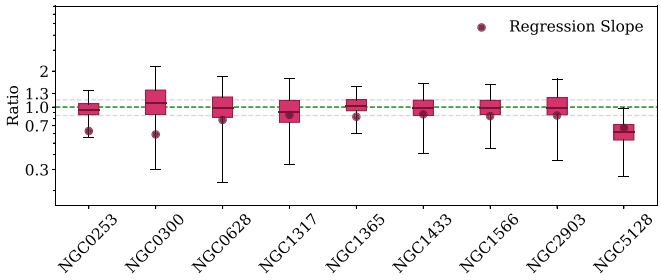

Figure 7. The same as Figure 6, but for AstroSat N219M to GALEX NUV maps.

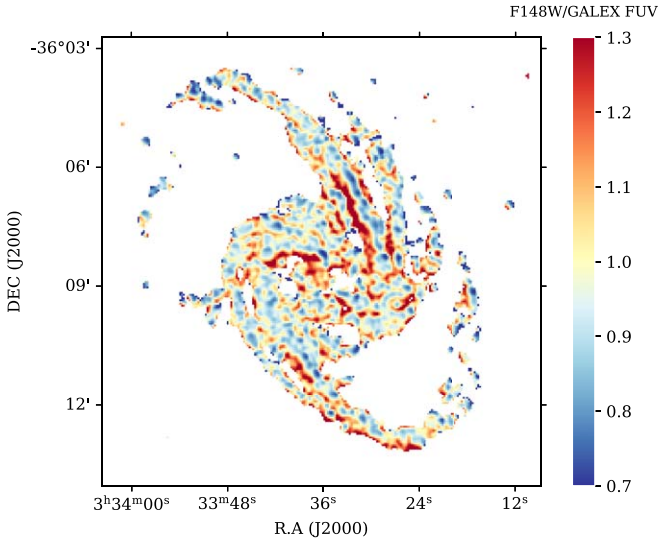

Figure 8. Ratio of AstroSat (F148W) to GALEX (FUV) in NGC 1365 at a common beam of 7.″5. The color bar at right shows the ratio values in a linear scale. We expect a ratio <1 (yellow to blue colors), as the central wavelength of the F148W filter is shorter than the GALEX band. As we discuss in Section 3.3.2, the slope of regression between AstroSat and GALEX $\beta = 0.92$ with an offset of 0.001 MJy sr^{-1}.

relation between data values and quantify any possible constant offsets between the data. After masking the values below 3σ for both AstroSat and GALEX maps at a common resolution, we find good agreement between the GALEX FUV and AstroSat F148W bands, with a median of $\beta = 0.92$ and with an offset of $C = 0.001$ MJy sr^{-1}, which is lower than the noise value by a factor of 2 in most targets. We expect a systematically lower fraction due to differences in the passband and central wavelength of F148W compared to the GALEX FUV filter ($\lambda_{\rm central} = 1528$ Å). In the NUV, we find a median of $\beta = 0.83$ and $C = 0.002$ MJy sr^{-1} among targets at the N219M band, which is reasonable given the difference with the GALEX NUV filter bandwidth and the central wavelength. We plot β values over the ratio of pixel value distribution for each galaxy in Figures 6 and 7 at the FUV and NUV bands, respectively. Figure 8 shows the ratio map of AstroSat F148W to GALEX FUV in NGC 1365 on a linear scale, where we see a good agreement at the 10% level across the galaxy.

4. XUV Disks

In the following sections, we illustrate the scientific potential of the arcsecond resolution and relatively wide FOV of the FUV imaging in the context of the PHANGS multiwavelength data set. Unlike the PHANGS observations conducted by ALMA, MUSE, JWST, and HST, which are predominantly confined to the inner disks of galaxies, AstroSat's observations extend significantly beyond the optical disks, offering a more expansive view of the low-density structure of galaxies (Leroy et al. 2021; Lee et al. 2022, 2023; Emsellem et al. 2022). Here, we use the AstroSat data to identify XUV disks beyond the optical disk of galaxies. Thilker et al. (2007) searched for XUV disk galaxies in the local Universe ($D < 40$ Mpc) using GALEX observations, finding UV-bright complexes beyond the optical radius in 30% of spiral galaxies (Thilker et al. 2007). The detection of XUV emission is particularly intriguing, as it implies the presence of recent massive star formation. Remarkably, this formation is taking place in poorly understood environments, characterized by low ISM pressure and low metallicity. These unconventional conditions foster extreme scenarios, which offer valuable opportunities to

Table 3
Adopted Galaxy Properties

Galaxy	SFR ($M_\odot$ yr^{-1})	Stellar Mass ($10^{10} M_\odot$)	Distance (Mpc)	Incl. (deg)	PA (deg)
IC 5332	0.47	0.41	9.01	26.9	74.4
NGC 0253	4.34	5.0	3.7	75.0	52.48
NGC 0300	0.18	0.15	2.09	39.8	114.3
NGC 0628	2.19	1.75	9.84	8.9	20.7
NGC 1097[a]	5.75	4.74	13.58	48.6	122.4
NGC 1300	4.14	1.17	18.99	31.8	278.0
NGC 1317	4.17	0.48	19.11	23.2	221.5
NGC 1365[a]	9.78	16.9	19.57	55.4	201.1
NGC 1385	0.95	2.09	17.22	44.0	181.3
NGC 1433	7.34	1.13	18.63	28.6	199.7
NGC 1512	5.16	1.28	18.83	42.5	261.9
NGC 1546	2.24	0.83	17.69	70.3	147.8
NGC 1566[a]	6.09	4.54	17.69	29.5	214.7
NGC 2090	1.09	0.41	11.75	64.5	192.46
NGC 2835	1.0	1.24	12.22	41.3	1.0
NGC 2903	4.3	3.08	10.0	66.8	203.7
NGC 3351	2.3	1.32	9.96	45.1	193.2
NGC 3621[a]	1.14	0.99	7.06	65.8	343.8
NGC 3627[a]	6.81	3.84	11.32	57.3	173.1
NGC 4254	2.66	3.07	13.1	34.4	68.1
NGC 4298	1.05	0.46	14.92	59.2	313.9
NGC 4321	5.56	3.56	15.21	38.5	156.2
NGC 4476	0.65	0.04	17.54	60.14	27.38
NGC 4535	3.4	2.16	15.77	44.7	179.7
NGC 4571	1.23	0.29	14.9	32.7	217.5
NGC 4579[a]	13.99	2.17	21.0	40.22	91.3
NGC 4654	3.69	3.79	21.98	55.6	123.2
NGC 5128	9.38	1.23	3.69	45.33	32.17
NGC 6744	5.29	2.41	9.39	52.7	14.0
NGC 7496[a]	0.99	2.26	18.72	35.9	193.7
NGC 7793	0.23	0.27	3.62	50.0	290.0

Note. The properties are taken from Leroy et al. (2021).
[a] These galaxies host an AGN based on Véron-Cetty & Véron (2010).

challenge and refine our current theories of star formation. Subsequent observations in the Local Volume and at a distance beyond 100 Mpc have further confirmed the ubiquity of XUV disk galaxies (Lemonias et al. 2011), reinforcing their importance in understanding galaxy evolution.

4.1. Background

There is some debate about what mechanisms power the XUV emission in galaxies, which could arise from different types of stars. Spectroscopic observations in M83 and NGC 4625 indicate that the emission of XUV disks ($>1.5R_{25}$) is linked to the population of young stars associated with low-mass stars (Gil de Paz et al. 2007b). Gil de Paz et al. (2007b) highlighted that the emission lines in the XUV disks of these galaxies are formed by single stars with masses between 20 and 40 $M_\odot$. Furthermore, their findings indicate that the role of planetary nebulae and blue-horizontal-branch (HB) stars in shaping XUV disks should be negligible. The highly excited gas of planetary nebulae and its high electron temperatures cannot explain the observed spectroscopic emission lines in XUV disks. On the other hand, the blue color of NUV–optical emission, as well as the structured shape of XUV disks (e.g., spiral arms), are pieces of evidence that do not support the role of HB stars as candidates for powering XUV disks (Gil de Paz et al. 2007b). Previous findings also confirm that FUV complexes with masses of $10^3 - 10^4\,M_\odot$ are being ionized by single stars (Gil de Paz et al. 2005). On the other hand, UV emission could also originate from white dwarfs in XUV disks (Sahu et al. 2019).

Different scenarios are proposed for triggering the star formation process in XUV disks, such as interactions, perturbations, and gas accretion (Bush et al. 2008, 2010; Das et al. 2021). In addition, spiral density waves could propagate from the inner to outer disk and result in gravitationally unstable regions that eventually form stars (Lemonias et al. 2011). As one possible indication of the formation mechanisms, radio observations also find extended H I disks associated with XUV emission in M83 and NGC 4625 (Tilanus & Allen 1993; Bush & Wilcots 2004; Bigiel et al. 2010a). In the case of the late-type galaxy NGC 0628, a faint trail of UV emission extends into the H I outer disk, which resembles a spiral-like structure (Das et al. 2020). This significant amount of H I is maybe due to a low-efficiency process of turning neutral gas into stars (Gil de Paz et al. 2007b). The consumption timescale of H I in XUV disks is estimated to range from a few gigayears up to the Hubble time (Gil de Paz et al. 2005). Galaxies hosting XUV disks might indicate the presence of molecular clouds as well as extended H I well beyond their stellar disks. The detection of faint CO emission in the outer disk is essential to understand the star formation efficiency (SFE) in this environment. For instance, Dessauges-Zavadsky et al. (2014) detected CO(1-0) in M63 with a low SFE, compared to inner disk regions, using the IRAM 30 m telescope. Koda et al. (2022) used deep ALMA observations to identify small molecular clouds associated with the XUV emission. The mechanisms behind the formation of XUV disks in galaxies are still unclear and the number of well-studied targets remains small. In this study, our objective is to use new UVIT observations to identify new potential candidates using the XUV disk classification scheme proposed by Thilker et al. (2007).

4.2. New Candidates

Following the prescriptions of Thilker et al. (2007) and Lemonias et al. (2011), we used a foreground-extinction-corrected, background-subtracted UV surface brightness ($\mu_{\rm FUV} = 27.25$ AB magnitudes arcsec^{-2}) as a threshold level to identify FUV clumps in XUV disks. This UV surface brightness corresponds to $\Sigma_{\rm SFR} = 3 \times 10^{-4}\ M_\odot\,{\rm yr}^{-1}\,{\rm kpc}^{-2}$, which is based on a Salpeter initial mass function (IMF) and calibrations from Kennicutt (1998). This type of XUV disk requires more than one structured UV complex (e.g., spiral segments) and is known as a Type 1 XUV disk or "M83-like" object. We do not consider diffuse UV emission as a criterion for XUV disks, as it could be related to other recent star formation processes or originated from hot core-helium-burning stars (Hoopes et al. 2005). On the other hand, Type 2 XUV disks are often dominated by a large, blue, low-surface-brightness (LSB) outer area with a higher specific SFR and less structured emission (see Section 3 in Thilker et al. 2007).

Using the radial profiles presented in Section 3.1, we measured the scale lengths of the FUV emission and CO molecular gas. Figure 9 compares the scale lengths of these two different data sets. On average, the scale length of the FUV ($\gamma_{\rm FUV} \simeq 3500$ pc) is about twice that of the CO molecular gas. These results indicate that the molecular gas is concentrated in

Table 4
Radial Profile Properties of Galaxies

Galaxy	$E(B-V)$ (mag)	$B_{\rm FUV}$ (10^{-18} erg s^{-1} cm^{-2} Å^{-1})	$\gamma_{\rm FUV}$ (kpc)	$\gamma_{\rm CO}$ (kpc)
IC 5332	0.02	0.07	4.3 ± 0.2	1.1 ± 0.1
NGC 0300[a]	0.01	0.08	...	1.4 ± 0.5
NGC 0628	0.07	0.07	5.2 ± 0.2	1.9 ± 0.2
NGC 1097	0.03	0.06	6.5 ± 0.7	1.9 ± 0.3
NGC 1300	0.03	0.08	4.6 ± 0.3	2.0 ± 0.6
NGC 1317	0.02	0.08	0.8 ± 0.1	0.6 ± 0.1
NGC 1365	0.02	0.05	8.3 ± 0.4	...
NGC 1385	0.02	0.09	1.5 ± 0.1	1.2 ± 0.1
NGC 1546	0.01	0.08	1.8 ± 0.1	...
NGC 1566	0.01	0.09	4.7 ± 0.2	2.2 ± 0.2
NGC 2090	0.04	0.15	5.6 ± 0.4	1.9 ± 0.6
NGC 2835	0.1	0.12	5.0 ± 0.5	2.1 ± 0.3
NGC 2903	0.03	0.07	4.0 ± 0.2	1.6 ± 0.1
NGC 3351	0.03	0.08	2.7 ± 0.1	1.5 ± 0.3
NGC 3621[a]	0.08	0.12	...	1.8 ± 0.2
NGC 3627	0.04	0.07	1.8 ± 0.1	1.9 ± 0.2
NGC 4298	0.04	0.07	1.9 ± 0.1	1.3 ± 0.2
NGC 4535	0.02	0.06	4.0 ± 0.2	2.7 ± 0.5
NGC 4654	0.03	0.07	3.6 ± 0.1	2.5 ± 0.1
NGC 5128[a]	0.1	0.18	...	0.8 ± 0.0
NGC 6744[a]	0.04	0.13	...	3.6 ± 0.4
NGC 7793	0.02	0.05	1.4 ± 0.1	1.2 ± 0.1
NGC 7496	0.01	0.07	1.7 ± 0.1	0.9 ± 0.1

Notes. Column (2): foreground color excess from Schlegel et al. (1998). Column (3): background emission at F148W. Column (4): scale length from the F148W band. Column (5): scale length from CO.
[a] The background ($B_{\rm FUV}$) is obtained from the "mean-level" method for these targets, described in Section 3.1, and no scale length is determined.

the stellar disk, while structured clumps of young massive stars, with a longer lifetime, can exist far beyond the optical disks. Significantly, as highlighted by Bigiel et al. (2010b), it has been observed that the scale length of H I is typically twice that of the FUV emission. Consequently, this leads to an extended depletion time for neutral gas, suggesting that XUV disk galaxies are frequently enveloped by extensive H I gas reservoirs. It is important to emphasize that the PHANGS-ALMA observations are primarily focused on the optical disk regions of galaxies, where the majority of massive CO clouds (with masses exceeding 10^4 $M_\odot$) are typically found. This emphasis is underscored by prior detections of CO in the XUV disks, where such clumps are often faint and isolated. Consequently, incorporating observations of diffuse clouds, which would requires deeper observations, is unlikely to significantly impact the determination of the CO scale lengths.

When comparing scale lengths, our focus was on identifying galaxies with large FUV scale lengths, particularly in comparison to the CO emission. Among the galaxies in our sample, NGC 6744 possesses the largest scale length, with $\gamma_{\rm FUV} = 9$ kpc and $\gamma_{\rm CO} = 3.8$ kpc. We note that the radial profile of this galaxy is not exponential, which has resulted in poor regression results, and hence the uncertainty is likely underestimated. We also observe that the obtained parameters of this galaxy, such as FUV scale length, amplitude, and background, are close to being outside of the reasonable range that we confined our initial regression parameters to. This is another indication that our regression does not adequately address the radial profile properties of this galaxy. Therefore, we did not use the background measured from the radial profile for this galaxy, as also noted in Table 4. This high-value FUV scale length is not surprising, as R_{25} is also more than 20 kpc in this galaxy. We investigate all targets with large $\gamma_{\rm FUV}$ relative to $\gamma_{\rm CO}$ and identify NGC 6744 and IC 5332 as also having FUV-bright segment structures beyond their optical disk, considering these as new candidates for XUV disks. We note that these targets are not covered in the previous studies of XUV disk galaxies by Thilker et al. (2007). We show the new XUV disk candidate galaxies in Figure 10 and discuss the features of these XUV disk galaxies below.

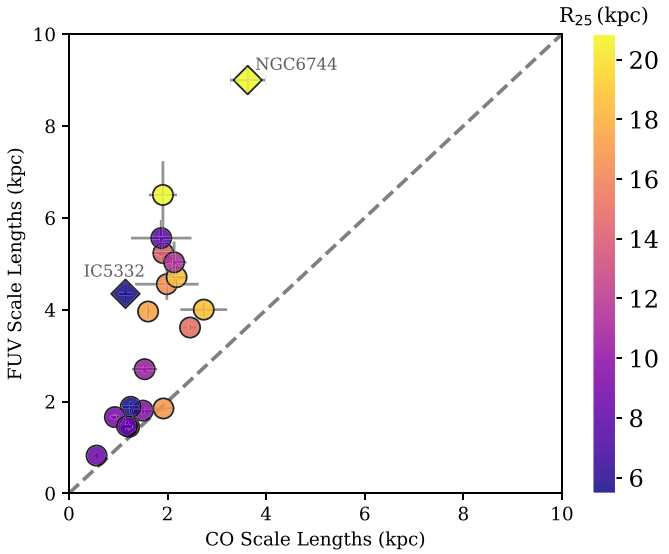

Figure 9. FUV F148W scale lengths vs. CO scale lengths obtained from radial profiles of galaxies, color coded with R_{25}. We show the two new XUV disk candidates with diamond markers.

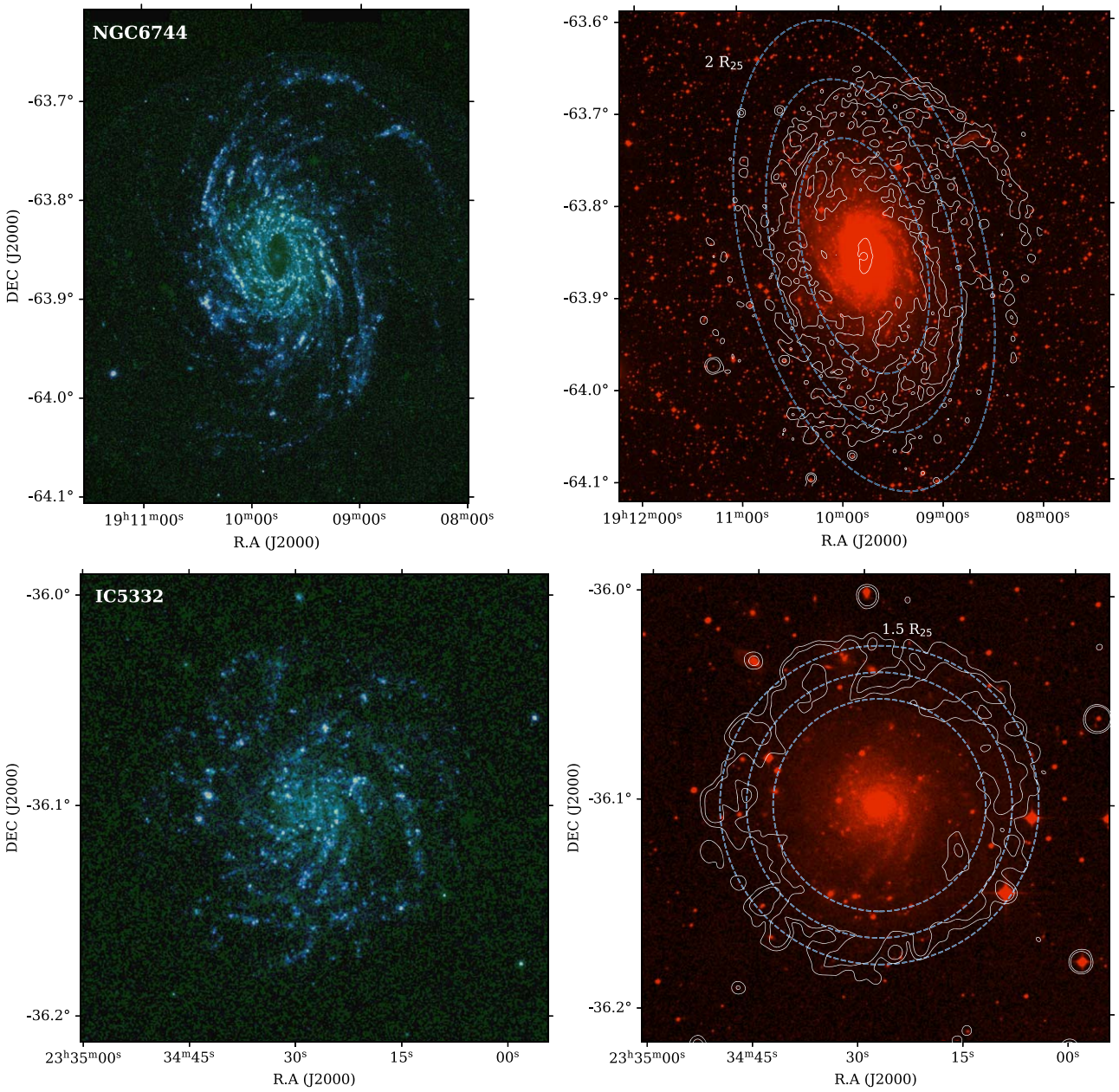

Figure 10. New candidates for XUV disk galaxies: NGC 6744 (top) and IC 5332 (bottom). Left: maps of AstroSat (F148W) in blue and 2MASS (K_s) in green at 2MASS resolution. The FUV map is in an asinh brightness scale. Right: Digitized Sky Survey 2 red map overlaid with the white contours of AstroSat F148W at levels of 26.2 and 27.9 M_{AB} for NGC 6744 and 27.2 and 28 M_{AB} for IC 5332. The FUV maps are not corrected for internal extinction. The blue ellipses are R_{25} with a 0.5 interval for NGC 6744 and 0.25 for IC 5332.

NGC 6744. This galaxy is an intermediate gas-rich spiral galaxy that hosts several FUV-bright clumps arranged in a spiral arm structure at a distance of approximately 29 kpc from its center. This galaxy is situated near the Galactic plane, which has led to it being less studied in surveys at other wavelengths, due to the observational complexities of observing at low Galactic latitude. However, we have identified two clearly visible FUV-bright spiral structures, both located beyond 1.5 times the optical radius ($1.5R_{25}$), without any corresponding bright optical counterparts. Interestingly, we do not see any bright 3.3 μm polycyclic aromatic hydrocarbon emission from the nearby stellar population in this area, as traced by IRAC 3.6 μm images (Fisher & Drory 2010 and references therein). Low-resolution H I observations also confirmed the presence of these two spiral arms, suggesting streaming motions along the H I arms as a result of interaction with a companion galaxy (Ryder et al. 1999). The companion IB(s)m NGC 6744A galaxy is visible in the northwest region in the FUV band as well. Furthermore, GMOS/Integral Field Unit observations in the center of this galaxy suggested two periods of star formation, with the last one happening one billion years ago, due to a merger event (da Silva et al. 2018). Having this evidence, we propose that NGC 6744 is a Type 1 XUV disk and its nature is probably related the accretion of gas from its companion in a merger event.

IC 5332. This galaxy is also another intermediate spiral galaxy, but with five times lower stellar mass ($M = 0.41 \times 10^{10}$ $M_{\odot}$) in comparison with NGC 6744. Although we see several star-forming complexes beyond the optical disk, we do not identify any ordered spiral-like features.

Unlike NGC 6744, there are several irregular clumpy structures at $R > R_{25}1.5$. Thilker et al. (2007) found that Type 2 XUV disks are more common in late-type/low-mass spirals, similar to IC 5332. Using Two Micron All Sky Survey K_s data from Skrutskie et al. (2006), we are unable to define an LSB zone for these irregular structures in the outer disk, as the K_s-band luminosity is faint in this region. Parkes and ATCA observations of IC 5332 also confirm the existence of an extended H I emission in the outer disk (Pisano et al. 2011). On the other hand, using the Hα emission map, we see a good match with the FUV emission (but not with old stellar population sites traced by IRAC 3.6 μm) in several clumps located in the southeast and west regions. These results might suggest an ongoing recent star formation process that results in diffuse UV emission and not an outer spiral arm feature. This scenario might cast doubt on IC 5332 being an XUV disk galaxy. Furthermore, being in the LGG 478 group of galaxies makes IC 5332 a possible part of a merger event. A detailed study of the star formation history in IC 5332 could shed light on understanding the different episodes of star formation and confirm such a scenario. The origin of the IC 5332 XUV emission remains unclear, but this target remains a candidate for an XUV disk.

5. Structural Measurements of FUV Emission

The motivation behind studying the clumping factor in CO and FUV emission is to understand the structure and distribution of molecular gas and newly born stars in galaxies. Leroy et al. (2013) indicate that models describing the structure of the ISM require detailed information on the mapping between the observed average surface density, referred to as the "area-weighted" surface density, at a resolution of a kiloparsec. This mapping plays a crucial role in comparing observations with theoretical models and enhancing our understanding of galaxy structure.

In this section, we explore the brightness distribution and emission structures of the FUV map as measured using the *clumping factor*. We compare the measures for FUV emission with the results for the CO. We contrast the clumping factor measurements with the results derived from the *Gini coefficient*, which can be used to characterize the structure of the emission in a map (e.g., Davis et al. 2022). Both the clumping factor and the Gini coefficient are scalar measurements of the shape of the probability density function.

5.1. Clumping Factor

The clumping factor is a scalar measurement that traces the width of the probability density function relative to its mean, which can be interpreted to measure the smoothness of the emission. We define the clumping factor following Leroy et al. (2013) and Sun et al. (2022):

$$c_{\mathrm{pix},\theta\ \mathrm{pc}} = \frac{\left(\sum_i I^2_{i,\theta\ \mathrm{pc}}\right) N_{\mathrm{pix}}}{\left(\sum_i I_{i,\theta\ \mathrm{pc}}\right)^2}, \tag{4}$$

where $I_{i,\theta\ \mathrm{pc}}$ is the surface brightness of region (i) at resolution of θ pc. The summation is over all pixels inside the region and N_{pix} is the total number of pixels inside that region. Equation (4) is the same definition from Leroy et al. (2013), where it is a ratio between the mass-weighted mean and the area-weighted mean of the surface density. The measurements from Leroy et al. (2013) indicate that molecular gas is highly clumped ($c \gtrsim 7$), whereas atomic gas has a smooth distribution ($c \approx 1$). This result could be interpreted as showing that most of the 21 cm emission originates from a diffuse medium with a high volume-filling factor (Leroy et al. 2013), while most of the molecular emission is organized into individual clouds. However, the UV clumping factor has not been examined before. The photospheric emission from young stars, traced by the FUV, should have slightly different clumping structures compared to molecular gas, since they are much brighter in the outer disk. Additionally, the FUV emission may originate from a wide range of stellar populations with different ages, so the clumping factor could lie between that of molecular and atomic gas. Here, we explore the clumpiness in the CO versus FUV emission to show how the formation of massive stars may derive from the ISM clumpiness. Having 31 galaxies spanning a wide range of mass and metallicity, we can also inspect the clumpiness in different galactic environments. We restrict our analysis to regions where the FUV maps overlap with the ALMA CO observations and carry out the analysis at a common resolution of 175 pc.

We use the environment masks from Querejeta et al. (2021) to measure the clumping factor in different morphological regions of galaxies. The environment masks include almost all morphological features of galaxies—most importantly, spiral arms, interarm regions, and centers. The masks were constructed using a visual inspection of the IRAC 3.6 μm data and structural decomposition analysis (Herrera-Endoqui et al. 2015; Salo et al. 2015). We note that the widths of the spiral arm masks are relatively broad (1–2 kpc) and are estimated from the spatial distribution of the CO emission.

We find that the median values of the clumping factor estimated from the FUV and CO emission are similar across most environment masks at a spatial resolution of 175 pc. This is illustrated in Figure 11, which shows the range of clumping factors seen in different galaxies that share common morphological features.

However, the center and spiral arms are the only regions that are more clumped in FUV relative to the CO. The median of the FUV clumping factor is 1.51, whereas the clumping factor for CO is 1.35 in the center of galaxies. To analyze the differences between these two distributions further, we applied the Kolmogorov–Smirnov (K-S) statistics. This analysis resulted in a K-S value of 0.4 in the center, indicating a modestly significant difference between the distributions, with a p-value of 0.04. In contrast, within the spiral arms, the median clumping factor is $c = 2.7$ for the FUV and $c = 2.5$ for CO. However, the K-S value in this region is lower than in the center, at 0.21. The associated high p-value of 0.92 shows no evidence for a significant difference between the FUV and CO distributions in the spiral arms. Consequently, this suggests that the distribution of the clumping factor for the FUV and CO in the spiral arms is more similar compared to the center.

The bars of galaxies have on average the largest clumping factor, particularly for the CO emission, with the CO clumping factor distribution reaching up to $\approx$7. This result is not surprising, since the most massive giant molecular clouds are located in bars (e.g., Rosolowsky et al. 2021), but these regions can also be devoid of molecular gas (Leroy et al. 2021). The CO emission in bars has also been shown to have a relatively thin structure (Stuber et al. 2023).

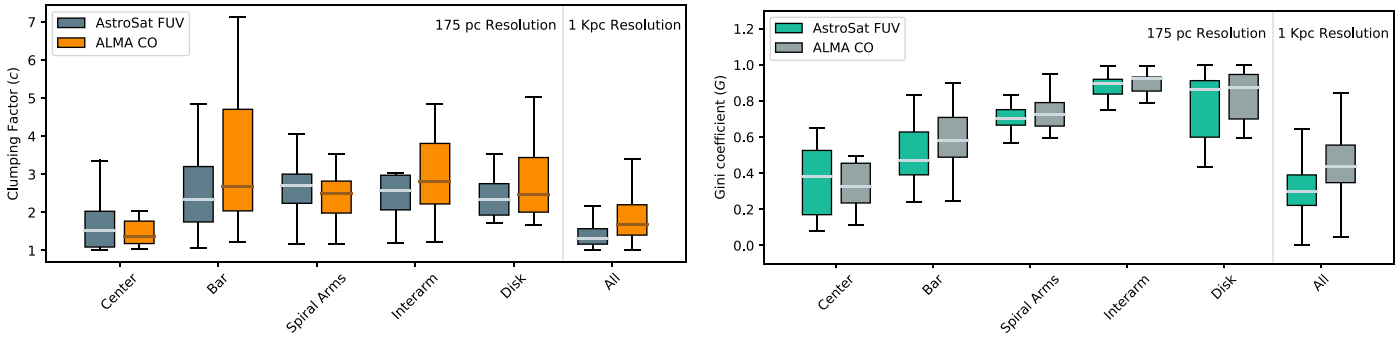

Figure 11. The lower and upper distributions of smoothness measurements of different morphological structures of galaxies at 175 pc resolution and 1 kpc size hexagonal apertures—the clumping factor (left) and Gini coefficient (right). The horizontal line inside each box plot represents the median value.

Using Table 3, we observed a higher $c_{\rm FUV}$ in the centers of galaxies hosting active galactic nuclei (AGNs). Notably, a similar trend was also seen in a few non-AGN galaxies.

On the other hand, spiral arms are more clumped in FUV emission, implying UV-bright complexes are more concentrated and molecular clouds are more uniformly spread along spiral arms. The clumping factor could also be exaggerated by high attenuation in the FUV band, broadening the distribution of light. Our results suggest that in general, clumps of molecular gas are more concentrated in galaxies, whereas FUV emission is more spread out at 175 pc resolution.

Figure 11 also shows the distribution of the measured clumping factor using 1 kpc size hexagonal apertures, labeled as "all." Similar to the galaxy-integrated values, the median CO clumping factor is still higher ($c = 1.7 \pm 0.1$) than the FUV values ($c = 1.3 \pm 0.1$). Our results are in good agreement with Sun et al. (2022), where they used highly sensitive ALMA observations of 90 nearby galaxies and reported $c_{\rm CO} = 1.9$ within hexagonal apertures. Leroy et al. (2013) reported a higher CO clumping factor ($c = 7$) at 20–300 pc resolution. One should account for the molecule-poor low-metallicity systems that Leroy et al. (2013) included in their sample, which usually have very high clumping factors. In contrast, the PHANGS-ALMA sample typically studies more distant, higher-mass systems (i.e., more metal-rich and bright in CO).

5.2. Gini Coefficient

We also use the Gini coefficient (G) as a nonparametric measure of the distribution of a quantity (Gini 1912). It has been adapted for quantitative morphological studies of galaxies at different wavelengths, including GALEX observations (e.g., Muñoz-Mateos et al. 2009). It measures the inequality in a distribution and the higher values indicate a concentration of medium brightness in a small region. The non-normalized values of the clumping factor might raise a concern where two different galactic environments exhibit similar values but not the same morphology. Hence, the Gini coefficient is considered here to assist us in distinguishing between the smoothness of different environments. Following Davis et al. (2022), we define the parameter as

$$G_{\theta\,\rm pc} = \frac{1}{\bar{I}\; n(n-1)} \sum_{i=1}^{n} (2i - n - 1) I_i, \qquad (5)$$

where n is a number of pixels, I_i is the surface brightness of each pixel sorted in ascending brightness order, and $\bar{I}$ is the mean brightness measured over all the pixels. The summation (i) is over all the pixels of the area. The Gini coefficient, with values between 0 and 1, measures the concentration of clumps in an area. A higher G value indicates a greater concentration of clumps. The accuracy of the G measurement can be influenced by factors such as the aperture size and the S/N of the data. If there are many faint pixels in the region, the results may be impacted (Lisker 2008). We present the distribution of the Gini coefficient in Figure 11. The median of the Gini coefficient measured in 1 kpc hexagonal apertures shows that our measurements of $G_{\rm CO} = 0.43$ are higher than $G_{\rm FUV} = 0.3$. This aligns with the clumping factor measurements, indicating that the UV emission is smoother at a kiloparsec resolution.

The Gini coefficient presents a complementary picture of smoothness of the ISM in galaxies compared to the clumping factor. As illustrated in Figure 11, the smoothness of both the CO and FUV emission decreases in parallel from the inside to the outer parts of galaxies. The centers exhibit a smoother distribution than the spiral arms and disks. We note that the high clumpiness measured by Gini in disks is due to the high level of noise in ALMA data at 175 pc. In spiral arms, there is no clear correlation between G and c, with G suggesting a more clumpy distribution. This discrepancy may be due to the sensitivity of G to the effect of faint diffuse emission in the spiral arms or the limited sample size (there are only 14 galaxies with spiral arm masks at this resolution). However, both measures find that the clumping of the CO and FUV emission is similar, with the CO being typically slightly more clustered than the FUV. Such a trend could be expected, given the typical "cycling" time of the molecular ISM (<30 Myr; Blitz & Shu 1980; Chevance et al. 2022) is less than the FUV emission that would be produced from the stars formed from the molecular clouds (100 Myr). Such clumping should be readily measured in simulations.

6. Comparing FUV and Hα Emission

In this section, we compare the FUV to the Hα emission in the resolved structure of galaxies. FUV and Hα are tracers of star formation on different timescales. The UV continuum arises primarily from the photosphere of O and B stars ($M > 3\,M_{\odot}$), sensitive to star formation over a 100 Myr timescale (Kennicutt & Evans 2012). In contrast, the Hα emission line originates from the recombination of gas that is ionized in H II regions by massive stars (EUV emission), which are typically only O and early-type B stars with masses of $M > 17\,M_{\odot}$ (Lee et al. 2009, 2011). The Hα emission line traces recent star formation with a timescale of about 5 Myr (Kennicutt & Evans 2012). Hence, the Hα emission is the

optical proxy for photons with $E_\gamma > 13.6$ eV but the AstroSat FUV data trace photons with $6 < E_\gamma/\mathrm{eV} < 9$.

Both tracers also suffer the effects of dust attenuation, but the attenuation toward the shorter wavelengths (FUV) is higher. Many studies (e.g., Calzetti et al. 1994; Kreckel et al. 2013) have observed that the nebular emission from dust-enveloped H II regions undergoes roughly double the reddening of the stellar continuum. As a result, the Hα attenuation is more comparable to the UV continuum, once differential reddening between gas and stars is factored in (Lee et al. 2009).

Utilizing the improved resolution from the AstroSat FUV observations, our goal is to compare these observations with PHANGS-MUSE Hα data (Emsellem et al. 2022). With 15 targets common to both data sets, we can probe the variation in the FUV-to-Hα ratio across distinct galactic environments at 175 pc and 1 kpc resolution. This ratio is influenced by a multitude of factors, such as the dust attenuation, age and mass of the stellar populations, star formation history, IMF, and metallicity (Lee et al. 2009).

The objective of this section is to examine the local variations of log FUV/Hα (hereafter, the "log ratio") with respect to the resolved structure of galaxies at a scale of 175 pc. Using the original unit of the UVIT maps (erg cm $^{-2}$ λ^{-1} s^{-1}), in this section, we express our results for the log ratio in terms of

$$\log\left(\frac{\mathrm{FUV}}{\mathrm{H}\alpha}\right) = \log_{10}\left(\frac{\lambda_{\mathrm{FUV}} F_{\mathrm{FUV}}/(\mathrm{erg\ s^{-1}\,cm^{-2}})}{F_{\mathrm{H}\alpha}/(\mathrm{erg\ s^{-1}\,cm^{-2}})}\right) \quad (6)$$

$$= \log_{10}\left(\frac{L_{\mathrm{FUV}}/(\mathrm{erg\ s^{-1}})}{L_{\mathrm{H}\alpha}/(\mathrm{erg\ s^{-1}})}\right), \quad (7)$$

where the λ_{FUV} is the central wavelength of the FUV filter used.

The aim is to build upon the previous study by Lee et al. (2009) on an integrated galaxy scale and understand which physical properties affect the log ratio on a subkiloparsec scale. Our analysis centers on the observed log FUV/Hα ratio, with an emphasis on the effect of attenuation. However, since we do not have NUV observations for all of our targets, we cannot independently assess the stellar attenuation at UV bands.

6.1. Environmental Dependency

We investigate the variation of the log FUV/Hα ratio across different environments by examining the distribution of the uncorrected log FUV/Hα ratio at resolutions of 175 pc and 1 kpc, as shown in Figure 12. The median of the log FUV/Hα ratio is approximately 2 across these environments. At the coarser 1 kpc resolution, the log ratio exhibits a median of 2.1 within hexagonal apertures for all targets. These observations align well with predictions from stellar population synthesis codes. In these models, the Hα flux is determined under the assumption of Case B recombination without flux leakage, and FUV fluxes are derived by stacking stellar spectra for each cluster. Notably, Hermanowicz et al. (2013) reported log FUV/Hα values in the range of 1.5–2.5.

The centers of galaxies have a median of log FUV/Hα = 1.7, the lowest among all environments, indicating the greater impact of dust attenuation, older stellar populations, or both. Furthermore, we found spiral arms exhibit a higher median log FUV/Hα = 1.9–2.0. The distribution of FUV/Hα is similar in interarm regions and disks, with a median of ∼2.1.

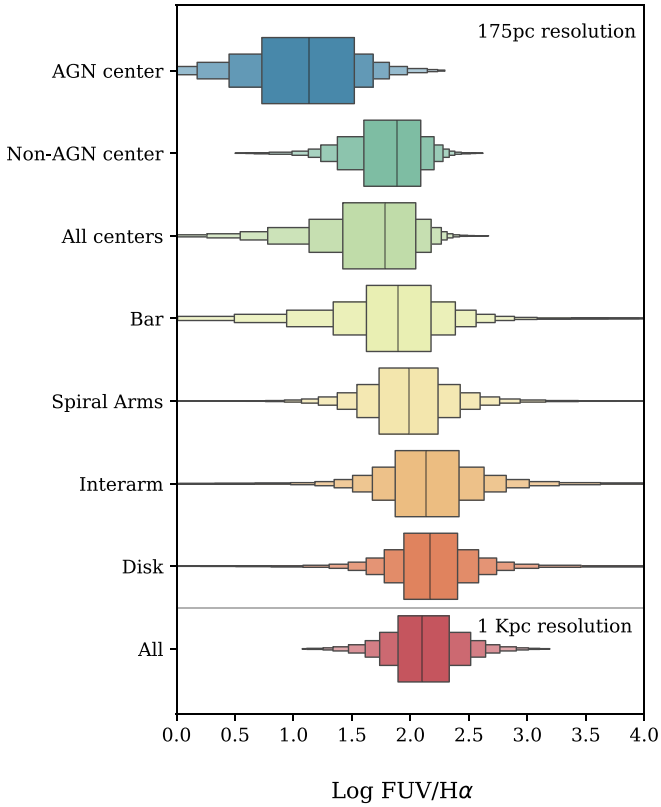

Figure 12. Distribution of the log FUV/Hα ratio across different morphological environments using both 175 pc resolution and 1 kpc hexagonal apertures (each box represents different quantiles of the ratio). The tails of the distributions reveal variations in fainter quantiles, particularly lower fractions in centers and bars. The median of each distribution is marked with a vertical line in the central quantile.

AGN-hosting galaxies, which were discussed in Section 5.1, also exhibit a lower log ratio (1.13) compared to non-AGN galaxies (1.88) in the center, although a direct connection between AGN activity and this ratio has yet to be established. Among the sampled galaxies, the center of NGC 1365 displays the lowest log ratio, with log FUV/Hα < 1. The classification of the central source in this galaxy, as provided by Querejeta et al. (2021), refers to an ellipse with a radius of more than 1.5 kpc, thereby encompassing the central star-forming ring. As highlighted by Whitmore et al. (2023), this central ring contains several bright, young star-forming regions, which are notably luminous in narrowband Hα HST maps (Ashley Barnes, private communication). This leads to an increased Hα emission in the center, with approximately 70% of this emission stemming from star-forming regions rather than the AGN. Therefore, the low FUV/Hα ratio observed in this region cannot be attributed exclusively to the AGN's influence. Further investigation of the inner 5″ (= 475 pc) of the NGC 1365 central source reveals a smooth non-star-forming disk, reminiscent of early-type galaxies. This region remains stable against gravitational collapse (Schinnerer et al. 2023). Other galaxies hosting AGNs, such as NGC 1566, NGC 3627, and NGC 7496, exhibit a log FUV/Hα ratio exceeding 1.4 in their centers. We note that the measurement of Hα in the center of AGNs can be challenging, as its spectra show broad features and multiple components that are not fitted by the single-Gaussian fitting approach used by Emsellem et al. (2022).

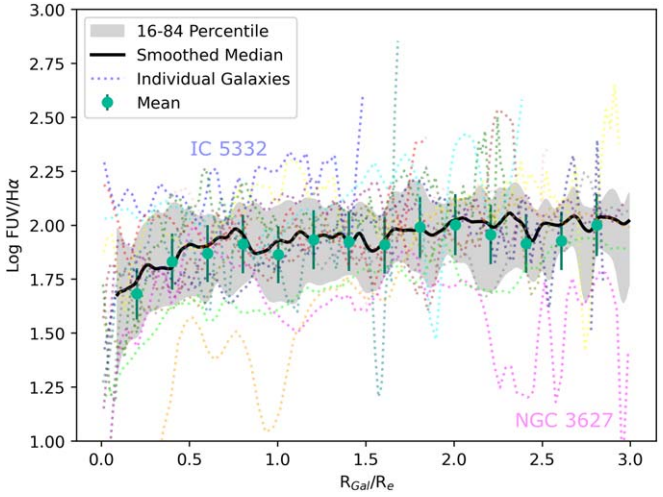

Figure 13. Gaussian-smoothed radial profile of log FUV/Hα for all galaxies at a resolution of 175 pc. The median values are represented by a black line, while the 16–84 percentile range of values is shown in gray. The mean of the smoothed profile is displayed as the green circles with error bars, taking into account uncertainties in both Hα and FUV. The radial profile of each galaxy is presented with a dashed line. The observations are limited to the FOV of MUSE. The radial profiles of two galaxies that do not exactly follow the median trend are highlighted and discussed in Section 6.2: IC 5332 (purple) and NGC 3627 (pink).

6.2. Radial Profiles

Figure 13 presents the variation of the log ratio with galactocentric radius scaled to the effective radius (R_e) for the 15 galaxies in the sample, obtained from Leroy et al. (2021). The median profile across all 15 targets is nearly flat, with a typical value of log FUV/Hα = 1.9, which is consistent with the analysis we provide in Section 6.1. Most of our targets have a flat radial profile, with a few spikes or dips. Most notably, the galaxies IC 5332 (log FUV/H$\alpha \sim 2.1$) and NGC 3627 (log FUV/H$\alpha \sim 1.65$) show a significant variation.

The low-mass spiral galaxy IC 5332, which is a candidate for a Type 2 XUV, as discussed in Section 4, shows a higher log FUV/Hα ratio. The majority of its H II regions have a ratio between 1.6 and 1.9, with a few regions exhibiting higher ratios (>2) in the spiral arm ends, indicating the presence of older populations. The higher ratio of log FUV/Hα is linked to the low dust content of IC 5332, where most of its H II regions display minimal reddening, $E(B-V) = 0.05$–0.1.

Conversely, NGC 3627, which extends up to 3 $R_{\rm Gal}/R_{\rm eff}$, demonstrates several dips in its radial profile, corresponding to various H II regions combined with a few Milky Way stars in its spiral arm. This combination results in a much lower ratio. The galaxy hosts a massive star-forming region located at the end of the bar, which shows higher reddening ($E(B-V) > 1$) and molecular gas ($I_{\rm CO}$>200 K km s^{-1}). In the central region, we observe a ratio of 0.7, which, once again, is associated with high reddening and a substantial amount of molecular gas. The H II regions display ratios of 0.9–1.1, often correlated with nearby bright molecular clouds with intensities of $I_{\rm CO}$>25 K km s^{-1}.

The nearly flat radial profile of the logarithmic ratio aligns well with the findings of Mehta et al. (2023). In their study, they investigated the dust-corrected FUV/Hα ratio in intermediate-mass galaxies (with stellar masses ranging from $10^{9.5}$ to $10^{10.2}$ $M_\odot$) at a redshift of approximately 1. They observed a similar trend persisting up to a normalized galactic radius of $R_{\rm gal}/R_{\rm e} < 1.6$.

6.3. Physical Parameters Affecting log FUV/Hα

Given the relatively high physical resolution of the PHANGS-AstroSat data set and the richness of the supporting data, we have a new opportunity to understand what physical factors are driving the changes in the log FUV/Hα ratios on 175 pc scales. These effects have been explored in previous works based on the integrated properties of galaxies or at coarser resolution (Lee et al. 2009; Meurer et al. 2009). While log FUV/Hα could provide good insight into galactic evolution through, e.g., tracing the star formation history (Lomaeva et al. 2022), the effects of dust attenuation and reddening will alter this ratio, so it is necessary to carefully understand the effects of dust. There are a myriad of possible factors shaping the FUV/Hα, so we assess whether these effects are detectable in our sample. In addition to those explored below, previous works have proposed several possible physical factors that change FUV/Hα, including the porosity of the ISM, stochastic effects from the number of massive stars, and variations in the IMF. Below, we focus our work on factors where we have good observational proxies.

Metallicity. Stellar populations with lower metallicity have hotter atmospheres, resulting in the production of more UV photons, particularly ionizing ones (Lee et al. 2009). Conversely, metal-rich populations, such as those concentrated in galaxy centers, tend to be cooler and more evolved, emitting a reduced amount of ionizing flux compared to the nonionizing UV continuum. Theoretical demonstrations by Lee et al. (2009), employing models from Bruzual & Charlot (2003), showed that the effect of metallicity primarily influences the Hα emission rather than the FUV emission, due to assumptions regarding case B recombination and the spatial treatment with ionizing photons. However, to observe this effect, one requires a significant variation in metallicity, so we expect this effect to be weak across our sample.

The EW of Hα. The EW of Hα is also used to trace the age of young stellar populations, particularly in areas where the Hα emission is bright enough (Scheuermann et al. 2023). The EW of Hα serves as an indicator of the relative brightness of the nebular emission compared to the underlying stellar continuum. Younger stars, with ages on the order of millions of years, exhibit high EW values for Hα, as they are actively ionizing the surrounding gas, producing intense nebular emission. Observations in both the local Universe and at higher redshifts confirm changes in the EW of Hα with the age of H II regions (e.g., Cedrés et al. 2005; Villar et al. 2011). On the other hand, evolutionary synthesis models have predicted its functional form (Zurita & Pérez 2008). The EW of Hα is a highly observable signature of the balance between very young and older stars. At the scale of H II regions, we expect to observe an anticorrelation between the EW of Hα and log FUV/Hα, where bright Hα is associated with ages below 10 Myr. For older stellar populations, where the EW of Hα is below 10 Å, the relation is not notable.

Star formation history. Sharp fluctuations in the SFR could also result in changes in the log FUV/Hα ratio, given the varying lifetimes of O and B stars. Consequently, this ratio may be used to trace variations in the SFR on different timescales, ranging from 5 to 200 Myr (Kennicutt & Evans 2012). This is often referred to as the "burstiness" of star formation. On the

other hand, a temporary decrease or "gasp" in the SFR should also be considered in this context (Meurer et al. 2009). Mehta et al. (2023) investigated the time evolution of the dust-corrected log FUV/Hα and found under conditions of steady, constant star formation that an equilibrium state is achieved with a log FUV/H$\alpha \sim 2$. This highlights how SFH parameters such stellar mass, age, and metallicity might impact the FUV/Hα ratio in galaxies.

Here we aim to quantify the relationship between log FUV/Hα and various observed quantities. Initially, we introduce a comprehensive model encompassing the majority of the observed and physical quantities to describe the log ratio as outlined in Section 6.3.1. Next, we present a simplified version of the model, wherein dust reddening emerges as the primary factor, accounting for 50% of the variation in the log ratio.

6.3.1. Drivers of the FUV/Hα Ratio

In this section, we present a comprehensive model to quantify the roles of different variables in predicting the log of the FUV/Hα ratio. Previous studies have demonstrated how various physical parameters of galaxies, specifically resolved structural parameters, can be modeled using multivariate linear regression in logarithmic space (e.g., Dey et al. 2019; Sun et al. 2022). We aim to predict log FUV/Hα using variables such as E($B-V$), $I_{\rm CO}$, Hα EW, stellar age, mass, and metallicity, using the panchromatic PHANGS data. Leveraging the PHANGS-MUSE observations, we employ maps of stellar mass, light-weighted age, and light-weighted stellar metallicity for our targets. The specific models used in that fit set the range of expectations for our results, which we summarize here. Specifically, they employ a *young* fitting template over the observed lines and continuum described in Emsellem et al. (2022). In that study, the E-MILES stellar population models from Vazdekis et al. (2016) and Asa'd et al. (2017) are expanded to include younger age groups. This is particularly important, as we are making a direct comparison of the ratio of young stellar populations traced by Hα at $<$5 Myr to intermediate ages traced by FUV emission. The selected templates incorporate the Padova isochrones and include 18 bins for ages ranging from 6.3 Myr to 14.12 Gyr. Here, we note that most of the ages measured from PHANGS-MUSE using the *young* template are older than 10 Myr, which does not align with the typical age of 5 Myr for Hα bright H II regions, as highlighted by Kennicutt & Evans (2012) and Hassani et al. (2023). Therefore, to more accurately trace the ages of these younger regions, we have incorporated the EW of Hα emission as a weighting factor in the Least Absolute Shrinkage and Selection Operator (LASSO) analysis. Additionally, the stellar metallicity is binned from -0.7 to 0.22 for older stellar populations (age $>$63 Myr), while for younger populations, the [Z/H] bins range from -0.7 to 0.41. Bright stars are masked in our results to avoid potential distortions. For our 175 pc resolution, we also include an environmental classification, which can assume values of 0 or 1. These environments are categorized as center, bar, spiral, interarm, and disk. We perform the same analysis for the 1 kpc scale, but exclude the environmental classifications, since the different environments are not well resolved at this resolution.

We note two important cautions here. First, we assume a linear relationship in log space between each predictor and the outcome variable, although we acknowledge that may not be the case. The combination of dust reddening with stellar mass, age, and metallicity may not exhibit a linear relation with the log FUV/Hα, especially at a 1 kpc scale. The interplay and degeneracy between dust, metallicity, and the age of stars has been addressed in previous studies (Lee et al. 2009). Moreover, due to this degeneracy, we anticipate colinearity between parameters, particularly between $E(B-V)$ and CO intensity, or age and metallicity. This colinearity will impact our results, as the coefficients of these parameters in the model will be influenced by each other.

Figure 14 highlights the correlation between different predictors. We observe a correlation between stellar metallicity and age, with a Spearman coefficient of approximately 0.6, indicating an older population with higher metal content. We also find a strong anticorrelation between the EW of Hα and the age of the stellar population. A similar anticorrelation is also observed between the EW of Hα emission and stellar metallicity. It is important to note that different environments do not exhibit any significant correlation with physical or observed parameters. However, we do observe a weak trend between the presence of a bar and the surface density of stellar mass, which can be attributed to the concentration of stellar gas in the bar of most galaxies (Stuber et al. 2023).

We use the LASSO regression (Tibshirani 1996) to understand how each predictor controls the variation of the log ratio. Following Dey et al. (2019), we use fivefold cross-validation (CV) to fine-tune the hyperparameters of the model, ensuring that the performance is evaluated on different subsets of the data. LASSO is a regularization method that helps prevent overfitting in linear regression models by introducing a penalty to the absolute sizes of the coefficients. This not only helps in model simplification, but also in feature selection, as some coefficients can be shrunk to zero, effectively excluding that predictor from the model. The degree of regularization is controlled by the parameter α. By adjusting the α value through CV, we make sure it provides the best fit between our training and validation data. This approach decreases the chances of overfitting and enhancing the simplification of the model. We apply the LASSO regression to our linear model, which is represented as

$$\log\left(\frac{\rm FUV}{\rm H\alpha}\right) = \alpha_0 + \sum_{i=1}^{n} \alpha_i [\log X_i - \log\langle X_i\rangle]. \quad (8)$$

Here, α_0 represents the intercept and α_i denotes the power-law exponents of our predictors. We standardize our predictors by normalizing by the median values of each variable ($\langle X_i\rangle$). As indicated by Equation (8), we use a log transform for all parameters, but we do not apply the transform for $E(B-V)$ and metallicity, which are already intrinsically logarithmic.

We present results of the regression at 175 kpc and 1 kpc resolution in Table 5. The intercept term (α_0) represents the expected log FUV/Hα when all predictors are equal to their medians, which is $\approx$2.0 at both resolutions. The slope coefficients indicate the change in the log FUV/Hα, while holding all other predictors constant. At 175 pc resolution, more localized effects and variations within resolved structures of galaxies may introduce additional complexities, which could account for the observed differences. In general, we observe negative exponents for all predictors, except for metallicity. A higher coefficient for dust reddening is observed at both resolutions, indicating the importance of attenuation in the log ratio. We also note that the slopes for the different environment predictors are all weak, suggesting that the variation in the log

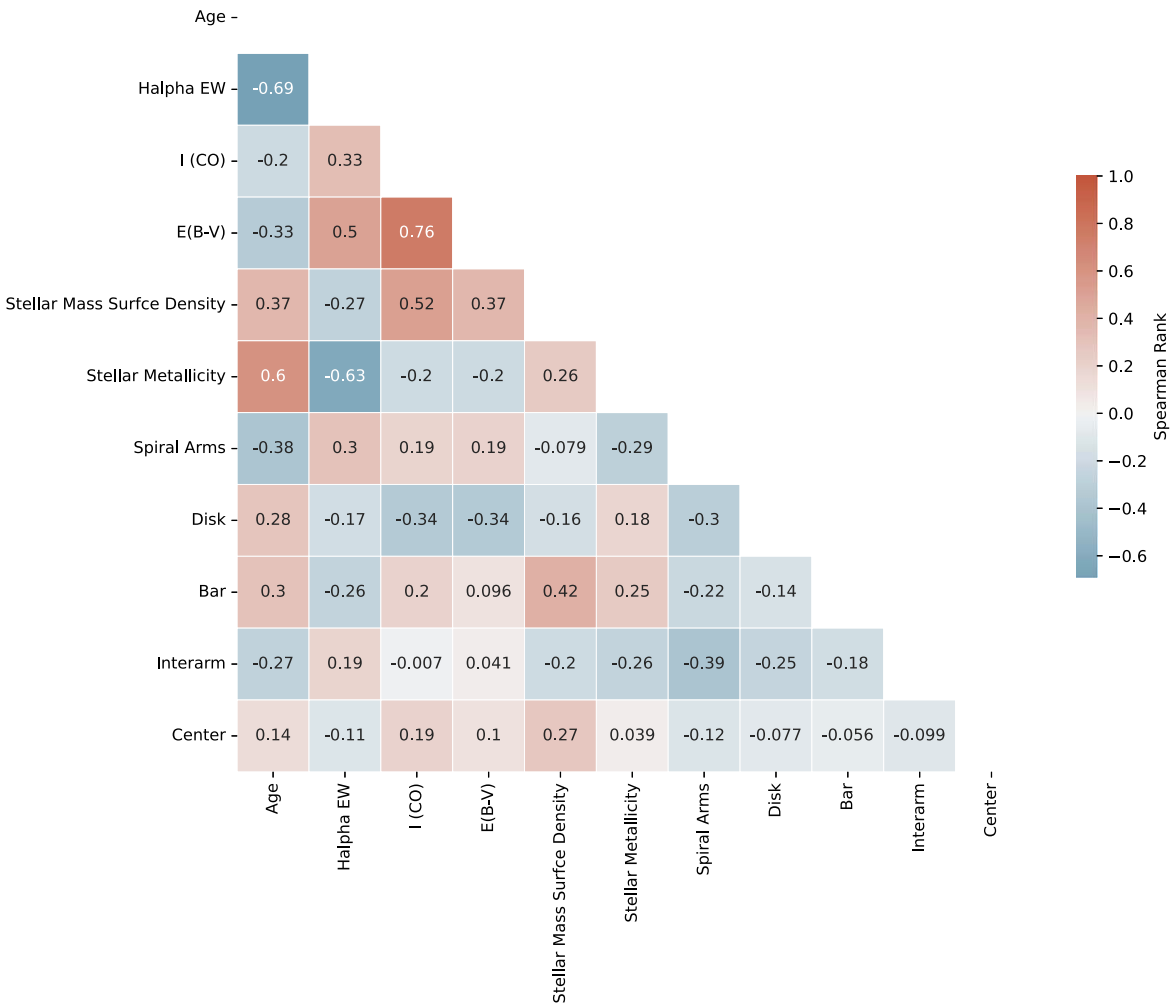

Figure 14. Spearman's correlation matrix illustrating the interrelationships between our predictor variables, analyzed at a resolution of 175 pc.

Table 5
The LASSO Regression Coefficients (α_i) for Different Predictors of log FUV/Hα at 175 pc and 1 kpc Resolution

Parameters	175 pc		1 kpc	
	Norm	α_i	Norm	α_i
$E(B-V)$	0.17 mag	-0.86 ± 0.01	0.11 mag	-0.61 ± 0.1
$I_{\rm CO}$	2.51 K km s^{-1}	-0.11 ± 0.01	1.75 K km s^{-1}	-0.10 ± 0.02
EW(Hα)	15 Å	-0.36 ± 0.01	11 Å	-0.46 ± 0.02
Age	615 Myr	-0.30 ± 0.01	707 Myr	-0.36 ± 0.03
$\Sigma_\star$	174 $M_\odot$ pc^{-2}	-0.07 ± 0.01	140 $M_\odot$ pc^{-2}	-0.18 ± 0.04
$[Z/H]$	-0.29 dex	0.06 ± 0.01	-0.22 dex	0.00
Environments[a]				
Center	⋯	-0.03 ± 0.01	⋯	⋯
Bar	⋯	-0.08 ± 0.01	⋯	⋯
Spiral	⋯	0.00	⋯	⋯
Interarm	⋯	-0.02 ± 0.01	⋯	⋯
Disk	⋯	-0.02 ± 0.01	⋯	⋯
R^2	0.67		0.66	
Residual (dex)	0.18		0.20	

Notes. The norm is the median of each predictor that we subtract in the log scale before regression. The residual value represents the scatter around the model, where we use the standard deviation to measure it. The variance inflation factor (VIF) for all parameters ranges from 2 to 3.7. Notably, the VIF for stellar mass is 5.8 at 1 kpc scale.

[a] Using environmental masks, we identify different morphological regions of galaxies and assign a weight of 0 or 1 to each individual part.

ratio we observe can be explained better by variations in other parameters in the model. Similarly, the scaling for metallicity (Z/H) is also weak, though the range of metallicities probed is relatively small.

Additionally, the Hα EW also exhibits a negative slope, suggesting that younger sources with prominent Hα EW values may result in a lower log FUV/Hα ratio. However, it is important to note that the relationship between the age of the stellar population and the Hα EW is not linear (Cedrés et al. 2005). We note the intrinsic correlation between the line brightness and its EW, which is tight in star-forming regions.

Furthermore, we observe a negative slope in the relationship between age and the FUV/Hα ratio, which is surprising. On the scale of H II regions or stellar clusters (i.e., <50 pc), we expect that a higher FUV/Hα ratio would correspond to an older population (i.e., >100 Myr), where the Hα emission is faint (Ujjwal et al. 2022). However, at a resolution of 175 pc, which is the best common resolution available, there might not be a clear relation due to the mixing of diffuse Hα emission with H II regions. Taking into account the degeneracy between age, metallicity, and dust attenuation, we propose that this negative slope may result from nonlinear relations between other parameters correlated with the stellar age. To clarify how this could have originated from the LASSO interpretation, we propose a simplified model to evaluate its performance in the next section.

To assess the uncertainty associated with the estimated coefficients in the regression results reported in Table 5, we employ a bootstrap resampling method. This approach involves generating multiple bootstrap samples by repeating the same LASSO regression with CV. We calculate the standard errors of the slopes by computing the standard deviation and across the iterations. Our findings reveal that the standard deviation on α_i at a scale of 1 kpc is below 0.1 for all predictors. Similarly, the standard deviations are below 0.01 at the 175 pc scale.

6.3.2. Simplified Model

The LASSO regression develops a multifactor model and the method does not isolate the drivers of the log FUV/Hα ratio automatically. However, it does show some factors have a stronger influence on the variation (large α_i) than others. Here, we develop a simple model that explains most of the variation in the FUV/Hα ratio.

The strongest factor in the analysis is dust attenuation, as measured by the color excess $E(B-V)$, suggesting the observed variations in FUV/Hα could be driven by attenuation alone. To delve deeper and find a simplified model to describe the log ratio, we run a model that includes only dust reddening, $E(B-V)$. This resulted in dust-reddening coefficients of approximately -1.7 at 175 pc scale. The goodness of fit, represented by R^2, yielded values of 0.5. This indicates that dust reddening alone can account for roughly half of the variation in the log ratio. Notably, a standalone model of CO can predict the log ratio as effectively as a single reddening component, with an R^2 of 0.4. However, the coefficient of the CO component is -0.4. Figure 15 illustrates that a lower log FUV/Hα ratio (indicating higher attenuation) corresponds to higher CO intensity, particularly in regions containing dense, dusty, and massive star-forming regions. This trend holds not only on the 1 kpc scale, as shown in Figure 15, but also at the 175 pc resolution. This suggests that dust and molecular emission are tracing each other. This supposition is borne out through measuring a significant correlation between CO emission and $E(B-V)$ on a kiloparsec scale, supported by a Spearman rank coefficient of $\rho \approx 0.75$. This correlation remains robust even when we enhance the resolution to 175 pc, although it exhibits notable variations across diverse environments.

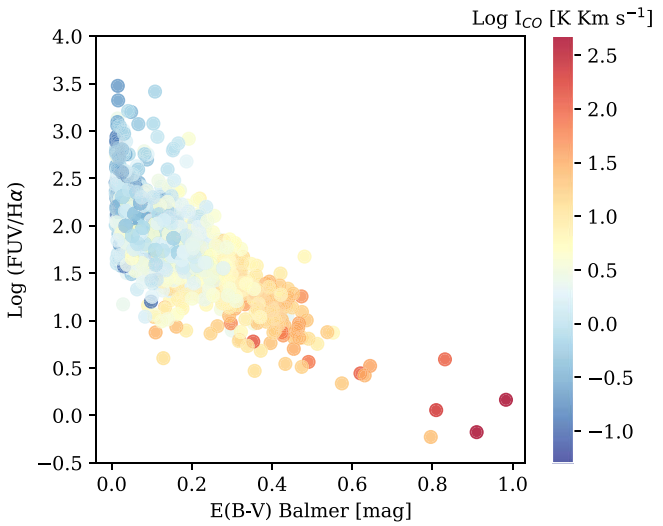

Figure 15. Log of FUV/Hα vs. the Balmer decrement $E(B-V)$ in 1 kpc size hexagonal apertures. The reddening is measured using MUSE/VLT observations in different galaxies. The color bar represents the CO(2−1) line integrated intensity. The figure shows that log FUV/Hα depends on both $E(B-V)$ and I_{CO}.

Furthermore, we find that the combination of reddening and Hα EW led to a better prediction of the model, increasing R^2 to 0.56. Interestingly, a model that includes only reddening and ages behaves very similarly, with the same R^2 as the previous model, indicating that Hα EW effectively traces the age of the stellar population. We note that even in the simplified models, the coefficient for age remains negative. Finally, including both age and Hα EW in the model increased both R^2 values to over 0.6, making them very similar to our comprehensive model. This also suggests that the inclusion of stellar mass, metallicity, and different environmental factors has a negligible effect on controlling the log ratio.

Based on the proposed simplified model of a single dust-reddening component, we have successfully predicted the FUV/Hα ratio with an $R^2 \sim 0.5$ at scales of 1 kpc and 175 pc, respectively. Subsequently, the simplified model exhibits higher scatter, approximately 0.2–0.25 dex, due to the inclusion of fewer parameters. However, the colinearity among various parameters complicates the interpretation of the individual effects of each parameter on the log ratio. We summarize the simplified models and their coefficients in Table 6.

6.3.3. Dust Attenuation Correction to FUV/Hα

As demonstrated in the previous section, dust attenuation is the primary factor governing variations in the uncorrected log FUV/Hα. In this section, we attempt to correct FUV/Hα for dust attenuation and explore which parameters exert the most influence on this log ratio.

Using the available NUV AstroSat observations for five of our targets, we first measure the slope of the UV continuum (β) to correct the FUV emission for internal attenuation. Following

Table 6
Regression Coefficients for Simplified Models Predicting log FUV/Hα

Parameters	Normalization	α_i	R^2
Observed FUV/Hα (175 pc scale)			
$E(B-V)$	0.17 mag	-1.68 ± 0.01	0.50
α_0	1.95		
I_{CO}	2.51 K km s^{-1}	-0.41 ± 0.01	0.41
α_0	1.94		
$E(B-V)$	0.17 mag	-1.22 ± 0.01	0.51
I_{CO}	2.51 K km s^{-1}	-0.15 ± 0.01	
α_0	1.95		
$E(B-V)$	0.17 mag	-1.38 ± 0.01	0.56
EW(Hα)	15 Å	-0.17 ± 0.01	
α_0	1.94		
$E(B-V)$	0.17 mag	-1.38 ± 0.01	0.64
EW(Hα)	15 Å	-0.34 ± 0.01	
Age	615 Myr	-0.34 ± 0.01	
α_0	1.93		
Attenuation-corrected FUV/Hα (1 kpc scale)			
Age	840 Myr	0.84 ± 0.02	0.49
Σ_*	168 $M_\odot$ pc^{-2}	-1.39 ± 0.02	
$[Z/H]$	−0.19 dex	0.33 ± 0.02	
α_0	2.98		

Boquien et al. (2012), we define β as follows:

$$\beta = \frac{\log(F_{FUV}/F_{NUV})}{\log(\lambda_{FUV}/\lambda_{NUV})} - 2, \quad (9)$$

with F representing the flux density and λ the central wavelength of the UVIT filter. We use a prescription following Boquien et al. (2012) to estimate A_{FUV} using our measured β values, thereby correcting the FUV emission. We also use the Balmer decrement measurements and $E(B-V)$ presented previously to correct the Hα emission, based on a typical value of the total-to-selective value $R_V = 3.1$ (Calzetti et al. 2000; Belfiore et al. 2023). After correcting both FUV and Hα, we measure the log ratio using 1 kpc hexagonal apertures and measure how well the variation of the ratio is predicted by the luminosity-weighted age, surface mass density, and metallicity of the stellar population. We found that this model can describe the variation of the dust-attenuation-corrected log ratio with an $R^2 = 0.49$. Our results show coefficients of 0.84 for age, −1.39 for the stellar mass surface density, and 0.33 for the stellar metallicity, along with an intercept of $\alpha_0 = 2.98$ (see Table 6). Similar to the approach used in Dey et al. (2019), we perform a partial regression and define the residual of this parameter (ΔlogFUV/Hα corrected) as:

$$\begin{aligned}\Delta \log(\mathrm{FUV}/\mathrm{H}\alpha)_{corr} = \log(\mathrm{FUV}/\mathrm{H}\alpha)_{corr} - \alpha_0 \\ -(-1.39 \log \Sigma_* - \langle \Sigma_* \rangle) \\ -(0.33[Z/H] - \langle [Z/H] \rangle),\end{aligned} \quad (10)$$

where $\langle \Sigma_* \rangle$ and $\langle [Z/H] \rangle$ are median normalization factors and α_0 is the intercept reported in Table 6 for the dust-attenuation-corrected log ratio. This relation effectively removes the influence of the stellar mass surface density and metallicity from the dust-attenuated log ratio and highlights its variation with age. Figure 16 shows the positive correlation between (ΔlogFUV/Hα corrected) and stellar age across five galaxies. The FUV emission can come from less massive stars with longer lifespans, unlike the more massive, short-lived stars (typically less than 10 million yr) responsible for Hα emission (Kennicutt & Evans 2012). Hence, the ratio should increase with the average age of a galaxy's stellar population, which in turn depends on the galaxy's star formation history.

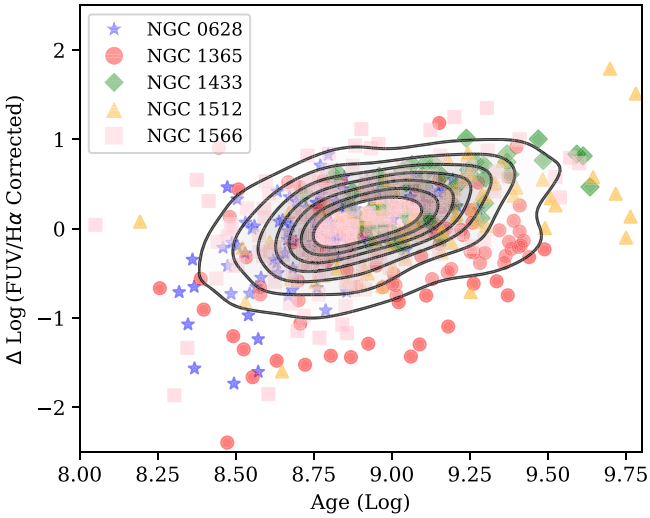

Figure 16. The residual values of log FUV/Hα vs. age, corrected for internal attenuation and adjusted by removing the influences of stellar mass and metallicity. The black contours show a kernel density estimation of the observed data set, focusing on the data distribution between the 16th to 84th percentiles. This relation includes measurements from only the five galaxies with NUV data available, which are necessary to measure the slope of the UV continuum and hence the FUV attenuation correction.

The star formation histories, whether constant or bursty, will further influence the evolution of the log ratio. After a burst of star formation, the FUV/Hα ratio will quickly rise, due to the sudden drop in Hα emission. Thereafter, the ratio will decrease again, moving toward an equilibrium value as the FUV-emitting stars eventually die. The models of Mehta et al. (2023) show that the log of the FUV/Ha ratio will reach an equilibrium state 100–200 million yr after the onset of a constant star formation history (see also the model predictions from Weisz et al. 2012 for log $M_\star \sim 10$ galaxies). The ages shown in Figure 16 show the luminosity-weighted measurements of ages from Emsellem et al. (2022), which trace the integrated star formation histories and show longer absolute timescales (log(age)∼9).

7. Conclusion

We present AstroSat UVIT observations of 31 massive spiral nearby galaxies spanning over an order of magnitude in stellar mass. These galaxies are part of the PHANGS survey of nearby galaxies that is synthesizing a broad range of multiwavelength data, including the ALMA and VLT/MUSE data that support this work. UVIT data improve over previous UV observations with ∼1.4″ resolution, enabling studies of young stellar populations and dust attenuation on <200 pc scales. This atlas contains data available from dedicated observations collected

as part of PHANGS, as well as a uniform reduction of the available data from the AstroSat archive. Hence, the atlas contains data from galaxies in one to nine UV bands covering wavelengths from 1480 to 2790 Å. These data can provide new resolved observational constraints to challenging questions, such as the attenuation curve, dust attenuation, and UV SFR for 30% of the full PHANGS sample. The PHANGS-AstroSAT atlas is available online at the CADC Data Publication Service at doi: 10.11570/23.0033. This paper describes:

1. *Observations and quality assessment.* The PHANGS-AstroSat atlas targets low-inclination ($i < 75°$), massive ($M_\star > 10^{9.57}\,M_\odot$), actively star-forming galaxies in the local Universe ($D < 22$ Mpc). As described in Section 2, we observe 11 galaxies for ∼3 ks each in the F148W band. For these and 20 other targets available in the archive, we apply the standard UVIT data calibration processes in CCDLAB (Section 3; Postma & Leahy 2017). We find that the pipeline reduction yields a typical resolution of 1.″4 at the FUV and 1.″2 at the NUV band. We provide science-ready maps of our targets after background subtraction and foreground extinction corrections. The UV background emission is $\sim 10^{-19}$ erg s^{-1} cm^{-2} Å^{-1} for most of our targets at $\lambda = 1480$ Å. We assess the quality of our data by comparing the AstroSat UVIT observations with GALEX maps from Leroy et al. (2019). The comparison of our data set with GALEX observations shows good flux scale agreement (<10% variations), as illustrated in Figures 6 and 7.
2. *XUV disks.* In Section 4, we present NGC 6744 as a new Type 1 XUV disk candidate and IC 5332 as a candidate for a Type 2 XUV disk galaxy. NGC 6744 shows a very large scale length in FUV and we identify two bright spiral arms beyond 1.5 R_{25}, without any R-band or Hα emission. We do not find convincing evidence of other candidates that were previously unknown, though we confirm all previous classifications (Thilker et al. 2007).
3. *Structure of CO and FUV emission.* In Section 5, we quantify the clumping and smoothness of the FUV and CO emission using two nonparametric scalar measurements: the clumping factor (c) and the Gini coefficient (G). Using more than 4000 hexagonal apertures of 1 kpc in size in our targets, we find $c_{\rm CO} = 1.7$ versus a median of $c_{\rm FUV} = 1.3$, illustrating the FUV emission is less clumped than the CO. In general, we find that bars are the most clumped environments. Although the median clumping factor from FUV and CO emission is similar across different environments, CO clumping factors are slightly higher than FUV except in the center and spiral arms. Furthermore, clumps of UV-bright emission, which could have H II region counterparts, have the most effect on increasing the clumping factor. The nonparametric Gini coefficient also predicts a smoother distribution for FUV emission compared to CO except in the center, which is in agreement with clumping factor results.
4. *FUV to Hα ratio.* In pairing UVIT and MUSE Hα maps, we used 1 kpc size apertures and see a ∼2 dex difference in the non-dust-corrected FUV and Hα luminosity (Section 6). We find $\log_{10}$(FUV/Hα) < 2 in the centers and bars. The log ratio at the center of AGN galaxies is 65% lower than that in normal star-forming galaxies. The radial profile of $\log_{10}$(FUV/Hα) is approximately flat outside the centers and shows small variation from 1.7 to 2.1. We propose an empirical model to predict the observed log ratio in our sample. The model considers how several parameters predict FUV/Hα, including CO molecular gas emission, $E(B-V)$, star formation history parameters (mass, age, and metallicity), and the EW of Hα. A full model is able to explain the variation of $\log_{10}$(FUV/Hα) at resolutions of 175 pc and 1 kpc, achieving approximately $R^2 \sim 0.65$. In evaluating different versions of the model, we argue that dust attenuation is the dominant factor controlling the variation of the log ratio in star-forming disk galaxies. Finally, having corrected both FUV and Hα emissions for internal dust attenuation, we find that when the influences of stellar mass and metallicity are excluded from the FUV/Hα log ratio, a positive correlation emerges between this ratio and the age of the stellar population.

The new perspective on star-forming complexes offered by AstroSat UVIT, when combined with our other ∼1″ resolution surveys, such as PHANGS-ALMA and PHANGS-MUSE, provides fresh insights on UV emission in nearby galaxies. Future work will be able to investigate hybrid UV+IR SFR calibrations, the attenuation curve, and the relation of the excess of dust to UV luminosity versus the stellar color (IRX–β) at subkiloparsec scales over a broad population of nearby galaxies.

Acknowledgments

We are grateful for the comments of an anonymous referee that improved the quality of this paper. This work was conducted as part of the PHANGS collaboration. This publication uses the data from the AstroSat mission of the Indian Space Research Organisation (ISRO), archived at the Indian Space Science Data Centre (ISSDC). H.H., E.R., J.N., E. W.K., and H.C. acknowledge the support of the Natural Sciences and Engineering Research Council of Canada (NSERC), funding reference number RGPIN-2017-03987, and the Canadian Space Agency funding reference Nos. SE-ASTROSAT19, 22ASTALBER, 19ASTROSA2, and 21EXPUVI3. E.W.K. acknowledges support from the Smithsonian Institution as a Submillimeter Array (SMA) Fellow and the Natural Sciences and Engineering Research Council of Canada. R.S.K. and S.C.O.G. acknowledge funding from the European Research Council via the ERC Synergy Grant "ECOGAL" (project ID 855130), from the German Excellence Strategy via the Heidelberg Cluster of Excellence (EXC 2181-390900948) "STRUCTURES," and from the German Ministry for Economic Affairs and Climate Action in project "MAINN" (funding ID 50OO2206). The team in Heidelberg is also grateful for the computing resources provided by *The Länd* and DFG through grant INST 35/1134-1 FUGG and for data storage at SDS@hd through grant INST 35/1314-1 FUGG. M. B. gratefully acknowledges support from the ANID BASAL project FB210003 and from the FONDECYT regular grant 1211000. J.M.D.K. gratefully acknowledges funding from the DFG through an Emmy Noether Research Group (grant number KR4801/1-1), as well as from the European Research Council (ERC) under the European Union's Horizon 2020 research and innovation program, via the ERC Starting Grant MUSTANG (grant agreement No. 714907). COOL Research DAO is a Decentralized Autonomous Organization supporting research in astrophysics aimed at uncovering our cosmic

origins. M.C. gratefully acknowledges funding from the DFG through an Emmy Noether Research Group (grant No. CH2137/1-1). H.A.P. acknowledges support by the National Science and Technology Council of Taiwan under grant 110-2112-M-032-020-MY3. K.K. and O.E. gratefully acknowledge funding from the Deutsche Forschungsgemeinschaft (DFG, German Research Foundation) in the form of an Emmy Noether Research Group (grant No. KR4598/2-1; PI: Kreckel) and the European Research Council's starting grant ERC StG-101077573 ("ISM-METALS"). K.G. is supported by the Australian Research Council through the Discovery Early Career Researcher Award (DECRA) Fellowship (project number DE220100766) funded by the Australian Government. K.G. is supported by the Australian Research Council Centre of Excellence for All Sky Astrophysics in 3 Dimensions (ASTRO 3D), through project number CE170100013. J.K. is supported by a Kavli Fellowship at the Kavli Institute for Particle Astrophysics and Cosmology (KIPAC). H.H. acknowledges the use of ChatGPT to refine the English-language presentation of the ideas in this paper.

Software: Python, Astropy (Astropy Collaboration et al. 2013, 2018, 2022), numpy (Harris et al. 2020), CCDLAB (Postma & Leahy 2017), spectralcube (Ginsburg et al. 2019), matplotlib (Hunter 2007), and ChatGPT.

Appendix A
Radial Profiles

Figure 17 presents the radial profiles for all PHANGS targets that are not presented in Figure 5.

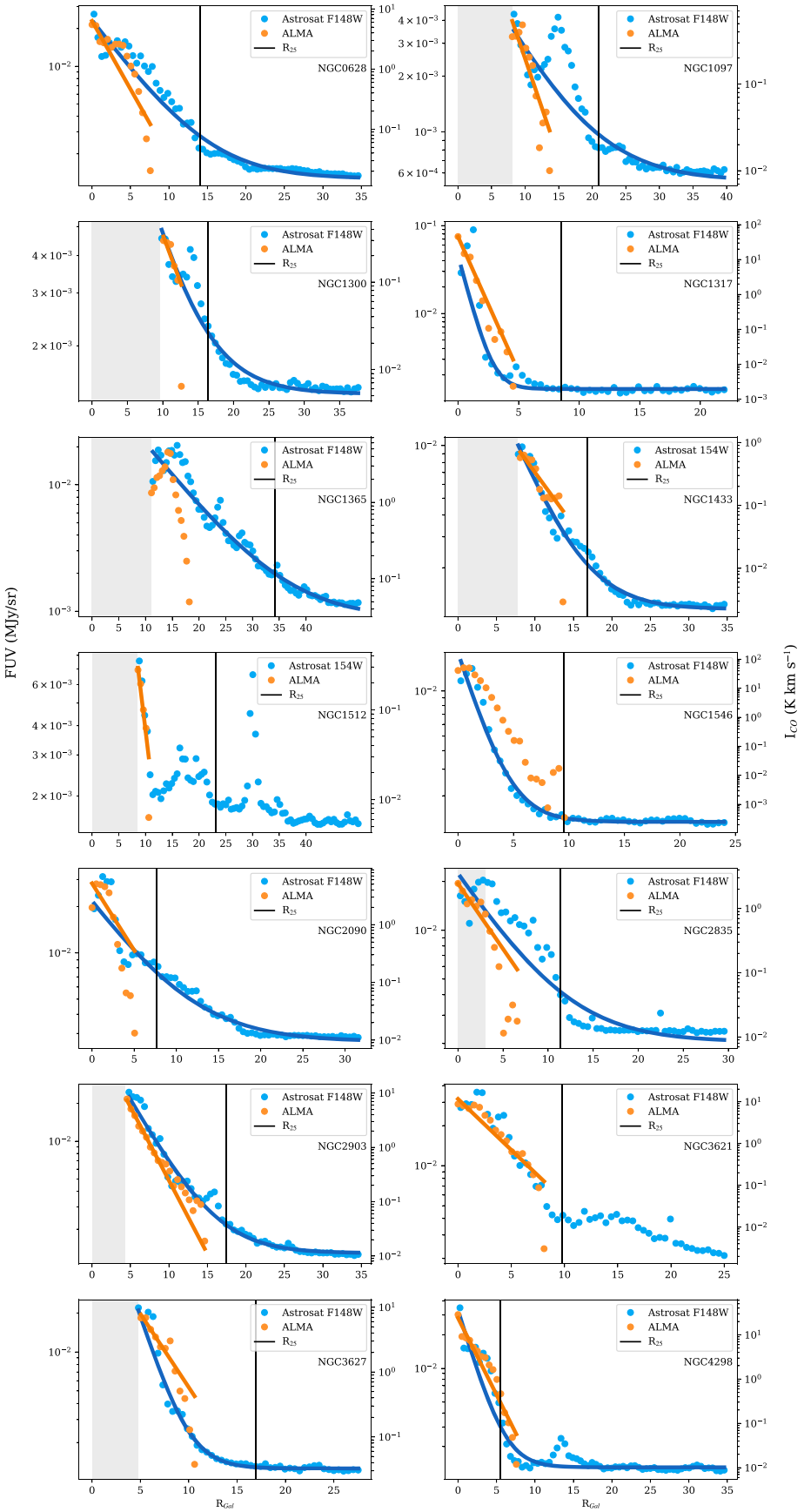

Figure 17. Radial profiles for all PHANGS targets that are not presented in Figure 5.

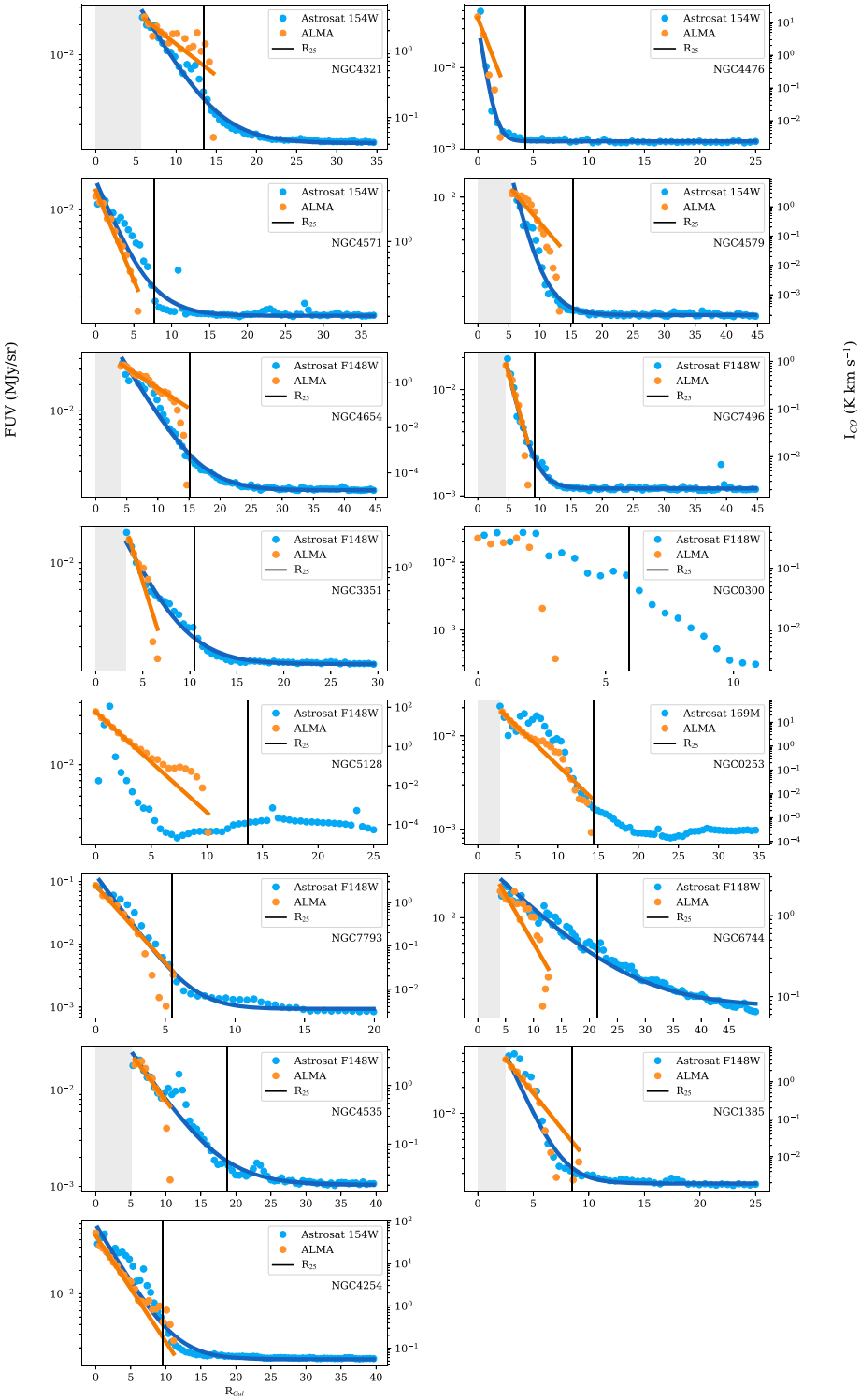

Figure 17. (Continued.)

ORCID iDs

Hamid Hassani https://orcid.org/0000-0002-8806-6308
Erik Rosolowsky https://orcid.org/0000-0002-5204-2259
Eric W. Koch https://orcid.org/0000-0001-9605-780X
Joseph Postma https://orcid.org/0000-0002-3025-1412
Joseph Nofech https://orcid.org/0000-0002-9553-953X
Harrisen Corbould https://orcid.org/0009-0007-7949-6633
David Thilker https://orcid.org/0000-0002-8528-7340
Adam K. Leroy https://orcid.org/0000-0002-2545-1700
Eva Schinnerer https://orcid.org/0000-0002-3933-7677
Francesco Belfiore https://orcid.org/0000-0002-2545-5752
Frank Bigiel https://orcid.org/0000-0003-0166-9745
Médéric Boquien https://orcid.org/0000-0003-0946-6176
Mélanie Chevance https://orcid.org/0000-0002-5635-5180
Daniel A. Dale https://orcid.org/0000-0002-5782-9093
Oleg V. Egorov https://orcid.org/0000-0002-4755-118X
Eric Emsellem https://orcid.org/0000-0002-6155-7166

Simon C. O. Glover https://orcid.org/0000-0001-6708-1317
Kathryn Grasha https://orcid.org/0000-0002-3247-5321
Brent Groves https://orcid.org/0000-0002-9768-0246
Kiana Henny https://orcid.org/0000-0001-7448-1749
Jaeyeon Kim https://orcid.org/0000-0002-0432-6847
Ralf S. Klessen https://orcid.org/0000-0002-0560-3172
Kathryn Kreckel https://orcid.org/0000-0001-6551-3091
J. M. Diederik Kruijssen https://orcid.org/0000-0002-8804-0212
Janice C. Lee https://orcid.org/0000-0002-2278-9407
Laura A. Lopez https://orcid.org/0000-0002-1790-3148
Justus Neumann https://orcid.org/0000-0002-3289-8914
Hsi-An Pan https://orcid.org/0000-0002-1370-6964
Karin M. Sandstrom https://orcid.org/0000-0002-4378-8534
Sumit K. Sarbadhicary https://orcid.org/0000-0002-4781-7291
Jiayi Sun https://orcid.org/0000-0003-0378-4667
Thomas G. Williams https://orcid.org/0000-0002-0012-2142

References

Asa'd, R. S., Vazdekis, A., Cerviño, M., et al. 2017, MNRAS, 471, 3599
Astropy Collaboration, Price-Whelan, A. M., Lim, P. L., et al. 2022, ApJ, 935, 167
Astropy Collaboration, Price-Whelan, A. M., Sipőcz, B. M., et al. 2018, AJ, 156, 123
Astropy Collaboration, Robitaille, T. P., Tollerud, E. J., et al. 2013, A&A, 558, A33
Belfiore, F., Leroy, A. K., Sun, J., et al. 2023, A&A, 670, A67
Bigiel, F., Leroy, A., Seibert, M., et al. 2010a, ApJL, 720, L31
Bigiel, F., Leroy, A., Walter, F., et al. 2008, AJ, 136, 2846
Bigiel, F., Leroy, A., Walter, F., et al. 2010b, AJ, 140, 1194
Blitz, L., & Shu, F. H. 1980, ApJ, 238, 148
Boquien, M., Buat, V., Boselli, A., et al. 2012, A&A, 539, A145
Bradley, L., Sipőcz, B., Robitaille, T., et al. 2020, astropy/photutils: 1.0.0, v1.0.0, Zenodo, doi:10.5281/zenodo.4044744
Bruzual, G., & Charlot, S. 2003, MNRAS, 344, 1000
Bush, S. J., Cox, T. J., Hayward, C. C., et al. 2010, ApJ, 713, 780
Bush, S. J., Cox, T. J., Hernquist, L., Thilker, D., & Younger, J. D. 2008, ApJL, 683, L13
Bush, S. J., & Wilcots, E. M. 2004, AJ, 128, 2789
Calzetti, D., Armus, L., Bohlin, R. C., et al. 2000, ApJ, 533, 682
Calzetti, D., Kinney, A. L., & Storchi-Bergmann, T. 1994, ApJ, 429, 582
Cedrés, B., Cepa, J., & Tomita, A. 2005, ApJ, 634, 1043
Chevance, M., Kruijssen, J. M. D., Krumholz, M. R., et al. 2022, MNRAS, 509, 272
Clark, C. J. R., Verstocken, S., Bianchi, S., et al. 2018, A&A, 609, A37
da Silva, P., Steiner, J. E., & Menezes, R. B. 2018, ApJ, 861, 83
Das, M., McGaugh, S. S., Ianjamasimanana, R., Schombert, J., & Dwarakanath, K. S. 2020, ApJ, 889, 10
Das, M., Yadav, J., Patra, N., et al. 2021, JApA, 42, 85
Davis, T. A., Gensior, J., Bureau, M., et al. 2022, MNRAS, 512, 1522
Decleir, M., De Looze, I., Boquien, M., et al. 2019, MNRAS, 486, 743
Dessauges-Zavadsky, M., Verdugo, C., Combes, F., & Pfenniger, D. 2014, A&A, 566, A147
Dey, B., Rosolowsky, E., Cao, Y., et al. 2019, MNRAS, 488, 1926
Emsellem, E., Schinnerer, E., Santoro, F., et al. 2022, A&A, 659, A191
Fisher, D. B., & Drory, N. 2010, ApJ, 716, 942
Gaia Collaboration, Vallenari, A., Brown, A. G. A., et al. 2023, A&A, 674, A1
Gil de Paz, A., Boissier, S., Madore, B. F., et al. 2007a, ApJS, 173, 185
Gil de Paz, A., Madore, B. F., Boissier, S., et al. 2005, ApJL, 627, L29
Gil de Paz, A., Madore, B. F., Boissier, S., et al. 2007b, ApJ, 661, 115
Gini, C. 1912, Variabilità e Mutabilità (Rome: Libreria Eredi Virgilio Veschi)
Ginsburg, A., Koch, E., Robitaille, T., et al. 2019, radio-astro-tools/spectral-cube: v0.4.4, Zenodo, doi:10.5281/zenodo.2573901
Harris, C. R., Millman, K. J., van der Walt, S. J., et al. 2020, Natur, 585, 357
Hassani, H., Rosolowsky, E., Leroy, A. K., et al. 2023, ApJL, 944, L21
Hermanowicz, M. T., Kennicutt, R. C., & Eldridge, J. J. 2013, MNRAS, 432, 3097
Herrera-Endoqui, M., Díaz-García, S., Laurikainen, E., & Salo, H. 2015, A&A, 582, A86
Hoopes, C. G., Heckman, T. M., Strickland, D. K., et al. 2005, ApJL, 619, L99
Hunter, J. D. 2007, CSE, 9, 90
Kennicutt, R. C., & Evans, N. J. 2012, ARA&A, 50, 531
Kennicutt, R. C., Jr. 1998, ARA&A, 36, 189
Khoperskov, S. A., & Vasiliev, E. O. 2017, MNRAS, 468, 920
Koda, J., Watson, L., Combes, F., et al. 2022, ApJ, 941, 3
Kreckel, K., Groves, B., Schinnerer, E., et al. 2013, ApJ, 771, 62
Kruijssen, J. M. D., Schruba, A., Chevance, M., et al. 2019, Natur, 569, 519
Krumholz, M. R., Bate, M. R., Arce, H. G., et al. 2014, in Protostars and Planets VI, ed. H. Beuther et al. (Tucson, AZ: Univ. Arizona Press), 243
Kulkarni, S. R. 2022, PASP, 134, 084302
Kumar, A., Ghosh, S. K., Hutchings, J., et al. 2012, Proc. SPIE, 8443, 84431N
Leahy, D., Buick, M., & Leahy, C. 2022a, AJ, 164, 183
Leahy, D., Seminoff, N., & Leahy, C. 2022b, AJ, 163, 138
Lee, J. C., Gil de Paz, A., Tremonti, C., et al. 2009, ApJ, 706, 599
Lee, J. C., Gil de Paz, A., Kennicutt, R. C., Jr., et al. 2011, ApJS, 192, 6
Lee, J. C., Sandstrom, K. M., Leroy, A. K., et al. 2023, ApJL, 944, L17
Lee, J. C., Whitmore, B. C., Thilker, D. A., et al. 2022, ApJS, 258, 10
Lemonias, J. J., Schiminovich, D., Thilker, D., et al. 2011, ApJ, 733, 74
Leroy, A. K., Lee, C., Schruba, A., et al. 2013, ApJL, 769, L12
Leroy, A. K., Sandstrom, K. M., Lang, D., et al. 2019, ApJS, 244, 24
Leroy, A. K., Schinnerer, E., Hughes, A., et al. 2021, ApJS, 257, 43
Leroy, A. K., Walter, F., Brinks, E., et al. 2008, AJ, 136, 2782
Lisker, T. 2008, ApJS, 179, 319
Lomaeva, M., De Looze, I., Saintonge, A., & Decleir, M. 2022, MNRAS, 517, 3763
Martin, D. C., Fanson, J., Schiminovich, D., et al. 2005, ApJL, 619, L1
Mehta, V., Teplitz, H. I., Scarlata, C., et al. 2023, ApJ, 952, 133
Meurer, G. R., Wong, O. I., Kim, J. H., et al. 2009, ApJ, 695, 765
Moffat, A. F. J. 1969, A&A, 3, 455
Muñoz-Mateos, J. C., Gil de Paz, A., Zamorano, J., et al. 2009, ApJ, 703, 1569
Peek, J. E. G., & Schiminovich, D. 2013, ApJ, 771, 68
Pisano, D. J., Barnes, D. G., Staveley-Smith, L., et al. 2011, ApJS, 197, 28
Postma, J. E., & Leahy, D. 2017, PASP, 129, 115002
Postma, J. E., & Leahy, D. 2020, PASP, 132, 054503
Querejeta, M., Schinnerer, E., Meidt, S., et al. 2021, A&A, 656, A133
Rahna, P. T., Murthy, J., Safonova, M., et al. 2017, MNRAS, 471, 3028
Rampazzo, R., Mazzei, P., Marino, A., et al. 2017, A&A, 602, A97
Ravishankar, B. T., Vaishali, S., Bhattacharya, D., et al. 2021, JApA, 42, 56
Regan, M. W., Thornley, M. D., Helfer, T. T., et al. 2001, ApJ, 561, 218
Roming, P. W. A., Kennedy, T. E., Mason, K. O., et al. 2005, SSRv, 120, 95
Rosolowsky, E., Hughes, A., Leroy, A. K., et al. 2021, MNRAS, 502, 1218
Ryder, S. D., Walsh, W., & Malin, D. 1999, PASA, 16, 84
Sahu, S., Subramaniam, A., Simunovic, M., et al. 2019, ApJ, 876, 34
Salim, S., Rich, R. M., Charlot, S., et al. 2007, ApJS, 173, 267
Salo, H., Laurikainen, E., Laine, J., et al. 2015, ApJS, 219, 4
Scheuermann, F., Kreckel, K., Barnes, A. T., et al. 2023, MNRAS, 522, 2369
Schinnerer, E., Emsellem, E., Henshaw, J. D., et al. 2023, ApJL, 944, L15
Schlegel, D. J., Finkbeiner, D. P., & Davis, M. 1998, ApJ, 500, 525
Singh, K. P., Tandon, S. N., Agrawal, P. C., et al. 2014, Proc. SPIE, 9144, 91441S
Singh, S., Ashby, M. L. N., Vig, S., et al. 2021, MNRAS, 504, 4143
Skrutskie, M. F., Cutri, R. M., Stiening, R., et al. 2006, AJ, 131, 1163
Stetson, P. B. 1987, PASP, 99, 191
Stuber, S. K., Schinnerer, E., Williams, T. G., et al. 2023, A&A, 676, A113
Subramaniam, A., Sindhu, N., Tandon, S. N., et al. 2016, ApJL, 833, L27
Sun, J., Leroy, A. K., Ostriker, E. C., et al. 2020, ApJ, 892, 148
Sun, J., Leroy, A. K., Rosolowsky, E., et al. 2022, AJ, 164, 43
Tandon, S. N., Postma, J., Joseph, P., et al. 2020, AJ, 159, 158
Tandon, S. N., Subramaniam, A., Girish, V., et al. 2017, AJ, 154, 128
Thilker, D. A., Bianchi, L., Meurer, G., et al. 2007, ApJS, 173, 538
Tibshirani, R. 1996, J. R. Stat. Soc. B, 58, 267
Tilanus, R. P. J., & Allen, R. J. 1993, A&A, 274, 707
Ujjwal, K., Kartha, S. S., Subramanian, S., et al. 2022, MNRAS, 516, 2171
Vazdekis, A., Koleva, M., Ricciardelli, E., Röck, B., & Falcón-Barroso, J. 2016, MNRAS, 463, 3409
Véron-Cetty, M. P., & Véron, P. 2010, A&A, 518, A10
Villar, V., Gallego, J., Pérez-González, P. G., et al. 2011, ApJ, 740, 47
Weisz, D. R., Johnson, B. D., Johnson, L. C., et al. 2012, ApJ, 744, 44
Whitmore, B. C., Chandar, R., Rodríguez, M. J., et al. 2023, ApJL, 944, L14
Zurita, A., & Pérez, I. 2008, A&A, 485, 5